The Global Monsoon Variability Simulated by CMIP3 Coupled Climate Models*

HYUNG-JIN KIM

International Pacific Research Center, School of Ocean and Earth Science and Technology, University of Hawaii at Manoa, Honolulu, Hawaii

BIN WANG

International Pacific Research Center, and Department of Meteorology, School of Ocean and Earth Science and Technology, University of Hawaii at Manoa, Honolulu, Hawaii

QINGHUA DING

Department of Meteorology, School of Ocean and Earth Science and Technology, University of Hawaii at Manoa, Honolulu, Hawaii

(Manuscript received 15 May 2007, in final form 13 March 2008)

ABSTRACT

The global monsoon climate variability during the second half of the twentieth century simulated by 21 coupled global climate models (CGCMs) that participated in the World Climate Research Programme's Coupled Model Intercomparison Project phase 3 (CMIP3) is evaluated. Emphasis was placed on climatology, multidecadal trend, and the response of the global monsoon precipitation to volcanic aerosols. The impact of the atmospheric model's horizontal resolution on the group ensemble mean (GEM; obtained from the three resolution groups) simulations of global monsoon climate is also examined.

The CMIP3 CGCMs' multimodel ensemble simulates a reasonably realistic climatology of the global monsoon precipitation and circulation. The GEMs are also able to capture the gross features of the global monsoon precipitation and westerly domains. However, the spreading among the rainfall GEMs is large, particularly at the windward side of narrow mountains (e.g., the western coast of India, the Philippines, Mexico, and the steep slope of the Tibetan Plateau). Main common biases in modeling rainfall climatology include a northeastward shift of the intertropical convergence zone (ITCZ) in the tropical North Pacific and a southward migration of the North Atlantic ITCZ during boreal winter.

The trend in the Northern Hemisphere land monsoon index (NHMI) detected in the CMIP3 models is generally consistent with the observations, albeit with much weaker magnitude. The significant decreasing NHMI trend during 1951–85 and 1951–99 occurs mainly in the models with volcanic aerosols (VOL models). This volcanic signal is detectable by comparison of the forced and free runs. It is estimated that from about one-quarter to one-third of the drying trend in the Northern Hemisphere land monsoon precipitation over the latter half of the twentieth century was likely due to the effects of the external volcanic forcings. On the other hand, the significant increasing trend in the global ocean monsoon index (GOMI) during 1980–99 appears chiefly in those models that are free of volcanic aerosols (No-VOL models). The exclusion of the volcanic aerosols is significant in simulating the positive GOMI trend against the internal variability of each model. These results suggest the climatic importance of the volcanic forcings in the global monsoon precipitation variability.

1. Introduction

The future spatiotemporal change in the global monsoon is one of the deepest concerns worldwide because the monsoon determines fundamental characteristics of the earth's climate and its rain provides a major water resource to more than two-thirds of the world's population. Coupled global climate models (CGCMs) have been used to predict future climate changes. However,

* School of Ocean and Earth Science and Technology Publication Number 7517 and International Pacific Research Center Publication Number 542.

Corresponding author address: Hyung-Jin Kim, International Pacific Research Center, University of Hawaii at Manoa, 1680 East West Road, Post Bldg. 401, Honolulu, HI 96822.
E-mail: hyungjin@hawaii.edu

DOI: 10.1175/2008JCLI2041.1

because of our limited knowledge of the highly complex climate system, determining the accuracy of the CGCMs' future projection remains a challenge (Covey et al. 2003; Meehl et al. 2005; AchutaRao and Sperber 2006; Joseph and Nigam 2006).

One way to improve the accuracy is to validate CGCMs' performance in terms of their simulations of the twentieth-century climate variations. A model's ability to realistically simulate the present climate is generally considered a "measure" of its capability to project the future. In this context, we will use the latest simulations by a suite of state-of-the-art CGCMs to assess their overall capability in reproducing the observed mean state and trend of the global monsoon precipitation and circulation.

Monsoons occur in various regions around the world. Each regional monsoon has its indigenous characteristics. At the same time, a regional monsoon system usually interacts with other monsoon(s) to some extent. For example, a strong South Asian summer monsoon tends to be followed by a strong Australian and weak eastern Africa monsoon during the subsequent boreal winter (e.g., Meehl 1997; Meehl and Arblaster 2002). Biasutti et al. (2003) have reported a close relationship between the South American monsoon and the African monsoon. Teleconnections between East Asian–western North Pacific summer monsoon and North American summer rainfall were also revealed (Wang et al. 2001; Lau and Weng 2002; Zhang et al. 2005). These global-scale connections suggest that a global perspective is more useful to evaluate the simulated monsoon climate in the CGCMs.

Because of the lack of observations over the tropical ocean, delineation of the global monsoon has been hampered. Wang (1994) attempted to identify the monsoon precipitation regime in the global tropics by use of outgoing longwave radiation data. Recently, Wang and Ding (2006, hereafter WD2006, 2008) proposed simple criteria to define the global monsoon domain and measure the global monsoon intensity. WD2006 further showed an overall *downward* trend in the monsoon precipitation over the global land monsoon regions during 1948–2003, but an *upward* trend in the monsoon precipitation over the global oceanic monsoon regions during 1979–2003. In this study, we will apply their metrics for demarcating the global monsoon domain and detecting the long-term variation of the global monsoon intensity to evaluate the performance of the 21 CGCMs that participated in the World Climate Research Programme's (WCRP's) Coupled Model Intercomparison Project phase 3 (CMIP3) multimodel dataset.

The solutions of the current CGCMs archived in the CMIP3 dataset display a wide range of skill in reproducing the monsoon rainfall variability over the various regions of the world. Annamalai et al. (2007) documented the diverse behavior of the modeled rainfall climatology over the South Asian monsoon region. The simulation of the East Asian monsoon precipitation showed considerable intermodel differences (Zhou et al. 2006). Lau et al. (2006) evaluated the CMIP3 model performance in capturing the recent Sahel drought signal and suggested physical mechanisms required for the realistic representation of the interdecadal rainfall variability over the African Sahel regions. While the majority of the previous studies have focused primarily on the reality of the regional monsoons, the accuracy of the simulated global monsoon climate as a whole has seldom been investigated. The present study, therefore, aims to address the following questions: 1) How well do the CMIP3 CGCMs simulate the observed climatology of the global monsoon precipitation and accompanied tropical circulation? 2) Can these CGCMs reproduce the observed rainfall and circulation trend over the global monsoon domain? 3) Does the model resolution affect the simulations of the global monsoon precipitation and circulation? 4) How does the global monsoon precipitation respond to natural volcanic forcing, and how significant is this volcanic signal against the natural variability?

The structure of the paper is as follows. Section 2 first describes the models and observational datasets. In section 3, the climatological aspects of the simulated global monsoon precipitation domain and associated precipitation are compared against observations, while in section 4 the simulated rainfall trend over the global monsoon precipitation domains is examined. Section 5 analyzes the tropical atmospheric circulation over the global westerly monsoon domain. In section 6, we present the response of the modeled global rainfall variability to volcanic aerosols and determine the significance of the volcanic signal against the internal variability of each model. The influences of model resolution on these simulations are discussed in sections 3–5. A summary of this work is given in section 7.

2. Model and validation datasets

We use the monthly rainfall and zonal winds dataset of the twentieth-century coupled climate model simulations (20C3M) for the period of 1950–99 collected from the CMIP3 multimodel dataset. The 20C3M simulations used late-nineteenth-century initial conditions and were executed to the end of the twentieth century, with historical anthropogenic and natural forcings. The external forcings resulting from atmospheric greenhouse gases and sulfate aerosols were prescribed across

the simulations. However, the inclusion/specification of the twentieth-century variations in solar and volcanic forcings, land cover, stratospheric ozone, and anthropogenic and natural aerosols vary widely among the models [see Table 1 in Phillips and Gleckler (2006) for details].

As of July 2006, 23 climate modeling groups worldwide have submitted more than one realization of the 20C3M integration. The simulation results from two participating groups, however, were excluded because one model did not cover the latter half of the twentieth century and the other showed very unrealistic amounts and patterns of rainfall. Table 1 presents a brief description of the model configuration.

The CGCMs are divided into three groups based on the atmospheric models' horizontal resolutions, which range from the lowest of 5.0° × 4.0° (longitude by latitude) to the finest of 1.125° × ~1.125°. The "LOW" group consists of six models with a number of grid points less than 5400. The "MED" group includes 10 models whose resolutions are in the range of approximately 7000–13 000 grid points. The five CGCMs in the "HIGH" group have more than 18 000 grid points. In general, the horizontal resolutions of the LOW, MED, and HIGH groups are 4°–5°, 2°–3°, and less than 2°, respectively. After grouping, model simulations in each group are interpolated onto each group's dominant grid system as follows: 5° × 4° for the LOW, 2.8125° × 2.8125° for the MED, and 1.875° × 1.875° for the HIGH groups. Finally, a group ensemble mean (GEM) is made for each group by averaging the interpolated model results. Table 1 also lists the number of realizations of each model.[1] For a single model's multiple realizations, their average is considered as one member of the GEM.

Ensemble average from four monthly precipitation datasets is used to validate simulated precipitation over the global land area. These datasets are from Delaware University (Legates and Willmott 1990), the Climate Prediction Center at the National Center for the Environmental Prediction (NCEP; Chen et al. 2002), the Global Precipitation Climatology Centre within the Variability of Analysis of Surface Climate Observation project (Beck et al. 2005), and the Climatic Research Unit (Mitchell and Jones 2005). The data are put on a 0.5° × 0.5° grid over the period of 1950–99. For the global ocean, the Global Precipitation Climatology Project (GPCP; Huffman et al. 1997) data over the period of 1979–99 are used. Simulated monsoon circulation in the models is evaluated against the NCEP–National Center for Atmospheric Research (NCAR) reanalyses (Kalnay et al. 1996) for the period of 1950–99.

[1] For zonal winds that were provided on 17 pressure levels, we used only the first realization of each model because of their huge data size.

3. Global monsoon precipitation climatology

Following WD2006, we define the global monsoon precipitation domain as the region where 1) *the annual precipitation range exceeds 180 mm* and 2) *the local summer precipitation exceeds 35% of annual rainfall*. Here, the "annual precipitation range" is defined by local summer minus winter mean precipitation, and the "local summer" is June–August (JJA) in the Northern Hemisphere and December–February (DJF) in the Southern Hemisphere. WD2006 demonstrated that the global monsoon demarcation obtained from this simple definition is highly comparable to the monsoon domain that was previously defined based on more complicated criteria of Wang and LinHo (2002). Using these criteria, we estimate the modeled global monsoon domains and their associated precipitation based on the 21 CGCMs' 50-yr climatology and we compare them with the observations. We begin our analysis by examining the climatological annual mean precipitation resulting from its importance in evaluating model performance.

a. Climatological annual mean precipitation

Figure 1 shows the climatological annual mean precipitation derived from the observations and the GEMs. All GEMs bear a resemblance to the observations in terms of spatial patterns, such as the heavy rainfall over the Indo-Pacific warm pool and tropical Maritime Continent, the sharp and narrow rainband in the intertropical convergence zone (ITCZ) and the South Pacific convergence zone (SPCZ), and the midlatitude storm tracks off the eastern coast of Asia and North America. The dry regions situated at the subtropical highs, North Africa, and the Middle East are also well reproduced in each GEM.

Substantial discrepancies, however, exist between the observations and the GEMs. Figure 2 presents the global distribution of the climatological annual mean precipitation biases. The biases show a common pattern for all three groups. The models tend to exaggerate the precipitation amount over the western Indian Ocean and the Maritime Continent, but underestimate it over the Indian subcontinent and the Bay of Bengal, the equatorial western Pacific warm pool, and Brazil. The enhanced precipitation over the subtropical central North Pacific and the reduced rainfall north of the equator indicate a slightly northeastward migration of the northern ITCZ in the models. The positive rainfall biases over tropical South Pacific and the negative bi-

TABLE 1. List of the 21 CGCMs used in this study and their configurations ordered by the number of atmospheric horizontal grids. Zonal wind data are not available for the ECHO-G. The fifth column shows each model's resolution group, with which the group ensemble mean is calculated.

CMIP3 designation; institution	Resolution: Atmosphere[a] (No. of grids)	Resolution: Ocean[b]	No. of runs[c]	Group[d]	Forcing[e]
Institute of Numerical Mathematics Coupled Model, version 3.0 (INM-CM3.0); Institute of Numerical Mathematics, Russia	5° × 4° (3240)	144 × 84	1	LOW	No-VOL
GISS Model E-H (GISS-EH); National Aeronautics and Space Administration (NASA) Goddard Institute for Space Studies, United States	5° × 4° (3312)	72 × 46	5	LOW	VOL
GISS Model E-R (GISS-ER); NASA Goddard Institute for Space Studies, United States	5° × ~4° (3312)	72 × ~46	8	LOW	VOL
Canadian Centre for Climate Modelling and Analysis (CCCma) Coupled General Circulation Model, version 3.1 (CGCM3.1; T47 resolution); Canadian Centre for Climate Modeling and Analysis (CCCMa), Canada	3.75° × ~3.75° (4608)	192 × 96	5	LOW	No-VOL
ECHO-G; Meteorological Institute of the University of Bonn, Germany, and Meteorological Research Institute of Korea Meteorological Administration, Korea	3.75° × ~3.75° (4608)	128 × 117	5	LOW	VOL
GISS-AOM; NASA Goddard Institute for Space Studies, United States	4° × 3° (5400)	90 × 60	2	LOW	No-VOL
L'Institut Pierre-Simon Laplace Coupled Model, version 4 (IPSL CM4); Institute Pierre Simon Laplace, France	3.75° × ~2.5° (6912)	180 × 170	1	MED	No-VOL
UKMO HadCM3; Hadley Centre for Climate Prediction and Research, Meteorological Office, United Kingdom	3.75° × 2.5° (7008)	288 × 144	2	MED	No-VOL
Flexible Global Ocean–Atmosphere–Land System Model gridpoint version 1.0 (FGOALS-g1.0); State Key Laboratory of Atmospheric Sciences and Geophysical Fluid Dynamics (LASG)/Institute of Atmospheric Physics, China	2.8125° × ~3° (7680)	360 × 170	3	MED	No-VOL
CGCM3.1 (T63 resolution); CCCMa, Canada	2.8125° × ~2.8125° (8192)	256 × 192	1	MED	No-VOL
CNRM-CM3; Météo-France/Centre National de Recherches Météorologiques, France	2.8125 × ~2.8125° (8192)	180 × 170	1	MED	No-VOL
MIROC3.2, medium-resolution version [MIROC3.2(medres)]; Center for Climate System Research (CCSR), National Institute for Environmental Studies (NIES), and Frontier Research Center for Global Change (FRGCG), Japan	2.8125° × ~2.8125° (8192)	256 × 192	3	MED	VOL
PCM; National Center for Atmospheric Research, United States	2.8125° × ~2.8125° (8192)	360 × 180	4	MED	VOL
MRI CGCM2.3.2a; Meteorological Research Institute, Japan	2.8125° × 2.8125° (8192)	144 × 111	5	MED	VOL
Geophysical Fluid Dynamics Laboratory Climate Model version 2.0 (GFDL CM2.0); U.S. Department of Commerce/National Oceanic and Atmospheric Administration (NOAA)/GFDL, United States	2.5° × 2.0° (12 960)	360 × 200	3	MED	VOL
GFDL Climate Model version 2.1 (CM2.1); U.S. Department of Commerce/NOAA/GFDL, United States	2.5° × ~2° (12 960)	360 × 200	3	MED	VOL
Commonwealth Scientific and Industrial Research Organisation Mark version 3.0 (CSIRO Mk3.0); Commonwealth Scientific and Industrial Research Organization, Australia	1.875° × ~1.875° (18 432)	192 × 189	3	HIGH	No-VOL
ECHAM5/Max Planck Institute Ocean Model (MPI-OM); Max Plank Institute for Meteorology, Germany	1.875° × ~1.875° (18 432)	360 × 180	3	HIGH	No-VOL
UKMO HadGEM1; Hadley Centre for Climate Prediction and Research, Meteorological Office, United Kingdom	1.875° × ~1.25° (27 840)	360 × 216	1	HIGH	VOL

TABLE 1. (*Continued*)

CMIP3 designation; institution	Resolution: Atmosphere[a] (No. of grids)	Resolution: Ocean[b]	No. of runs[c]	Group[d]	Forcing[e]
CCSM3; National Center for Atmospheric Research, United States	1.40625° × ~1.40625° (32 768)	320 × 395	5	HIGH	VOL
MIROC3.2(hires); CCSR, NIES, and FRCGC, Japan	1.125° × ~1.125° (51 200)	320 × 320	1	HIGH	VOL

[a] Longitude by latitude.
[b] Number of grids in longitude and latitude.
[c] The number of realizations for some models is different from that of the original ones, because of the missing values in the realizations that are excluded from this study.
[d] Interpolated grid systems are 5° × 4°, 2.8125° × 2.8125°, and 1.875° × 1.875° for LOW, MED, and HIGH, respectively.
[e] Historic volcanic forcing.

ases over subtropical South Pacific suggest that the so-called double-ITCZ problem (Mechoso et al. 1995) still exists in most CGCMs. Dai (2006) pointed out that the CMIP3 models without flux correction, which make up the majority of the CGCMs used in this study, tend to show an unrealistic double-ITCZ pattern resulting from the excessive expansion of the simulated cold tongue of sea surface temperature (SST) over the equatorial central Pacific.

It is also worth noting that the tropical Atlantic Ocean shows a biased pattern asymmetric about the equator. The models produce larger-than-observed rainfall in the South Atlantic, but underpredict it over the North Atlantic. This is because, while the observed

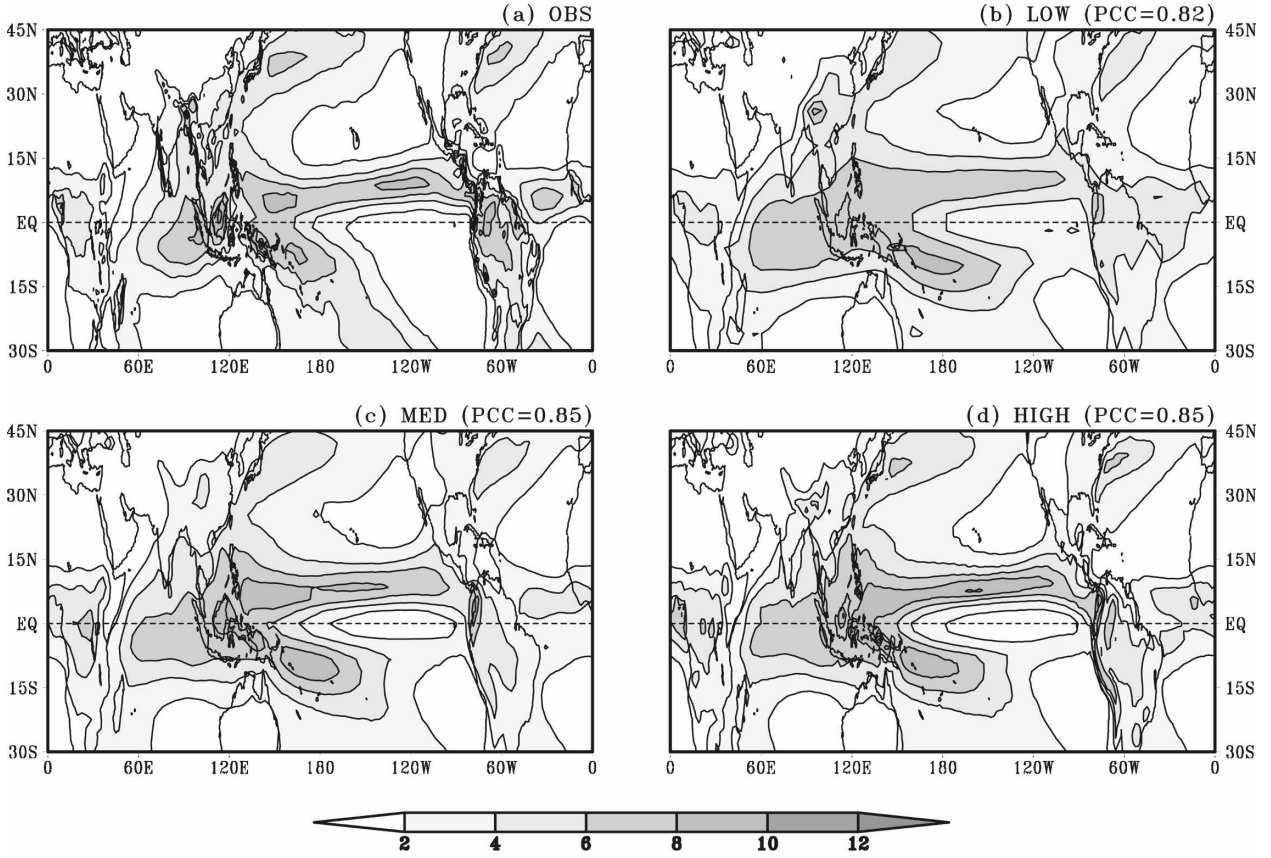

FIG. 1. Climatological annual mean precipitation (mm day^{-1}). (a) Observations, the group ensemble means of the (b) LOW, (c) MED, and (d) HIGH CGCMs. PCCs between the observations and the group ensemble means are shown at the upper-right corner of each figure.

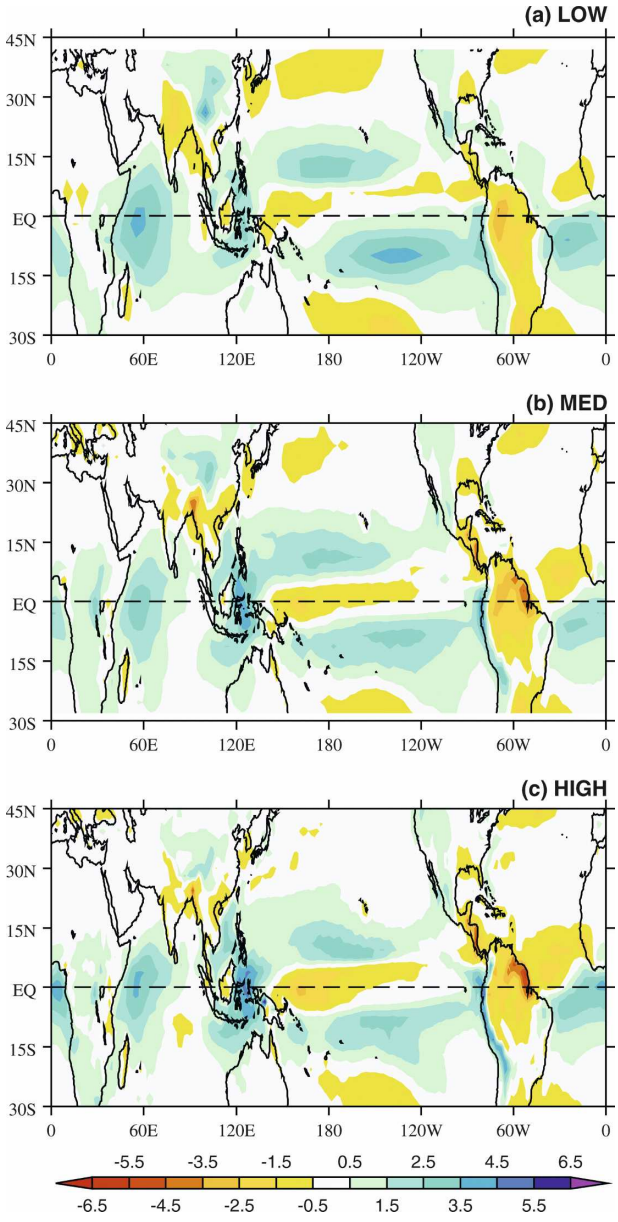

FIG. 2. Climatological annual mean precipitation biases (mm day^{-1}) from (a) LOW, (b) MED, and (c) HIGH.

Atlantic ITCZ usually stays at the equatorial North Atlantic Ocean all year-round (Fig. 1a), the modeled one tends to straddle the equator with an unrealistic broad rainbelt (Figs. 1b–d). The seasonal march of the Atlantic ITCZ in the models is found to be responsible for these systematic biases. The details about the simulated Atlantic ITCZ are discussed in the next section.

b. Climatological global monsoon domain and seasonality of rainfall

The basic characteristics of the monsoon climate are the seasonal reversal of wind direction and the rainfall contrast between the wet summer and dry winter. The annual precipitation range (AR) is one of the simplest measures of the monsoon rainfall's seasonality. Figure 3 compares the global distribution of the climatological AR (shadings) derived from the observations and the GEMs. The global monsoon demarcation established by the above-mentioned criteria is also depicted in Fig. 3 (contours). Major monsoon regimes in the observations include the following: the Asian, Indonesia–Australian, North and South African, and North and South American monsoons (Fig. 3a). Overall, these monsoon regions are apt to locate at each side of the equatorial perennial rainfall regions (Fig. 1).

The simulated global monsoon precipitation domains reproduce the observed major monsoon systems across the globe. The regional details of the simulated monsoon domain and AR, however, exhibit marked differences among the GEMs. For the South Asian monsoon, for example, the observed active AR centers are found at the western Indian coast, the eastern Bay of Bengal, and the South China Sea. The AR is, to a large degree, determined by the local summer rainfall. The factors that determine the distribution of the summer rainfall include the effects of orographic forcing, land–sea thermal contrast, and the conservation of the potential vorticity in the cross-equatorial flows (Rodwell and Hoskins 2001). The GEM of the LOW group (Fig. 3b) misses the centers of the AR at the western Indian coast and the South China Sea, which coincides with the windward side of the mesoscale terrain where orographic lifting due to monsoon flows induces intense convection (Chang et al. 2005; Xie et al. 2006). Meanwhile, the finer-resolution groups are able to capture the observed AR intensity and patterns reasonably well (Figs. 3c,d). In particular, the improvements of the AR in the MED and HIGH GEMs are found in the upstream regions of the mesoscale mountains, where the GEM of the LOW group is seen to be somewhat skill-less. Thus, a higher resolution yields better simulation near the narrow topography. The effects of the refined terrain in a model can also be seen along the steep slope of the Himalayas; as the resolution increases, the boundary of the simulated monsoon domains reaches farther westward, matching gradually well with the observations.

The North American monsoon domain also benefits from the increased resolution. The observed North America monsoon domain includes the west of the Sierra Madre Occidental along the west coast of Mexico where narrow mountains usually entail strong convection (Douglas et al. 1993). The simulation of the North American monsoon domain seems to be systematically improved with increasing resolution. Accordingly, the monsoon boundary in the HIGH group realistically

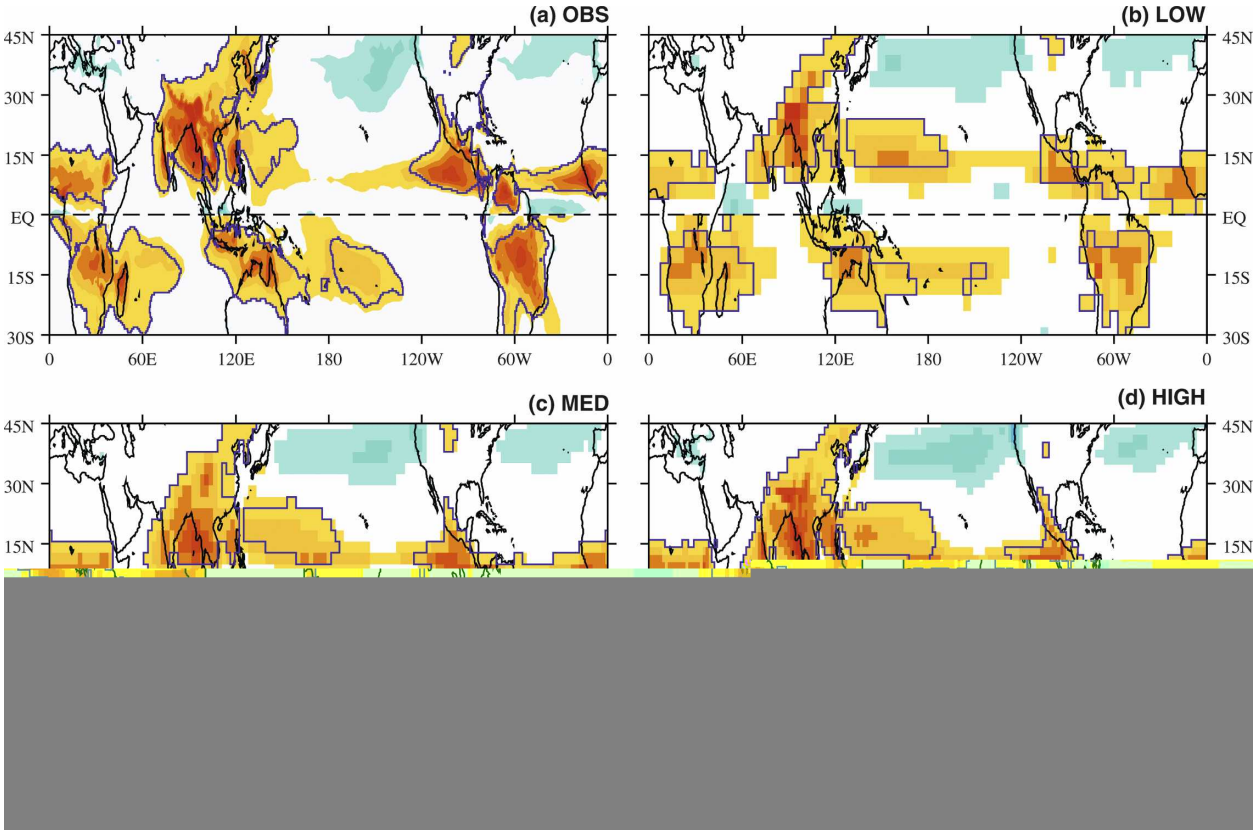

FIG. 3. Climatological annual precipitation range (shading; mm day^{-1}) and monsoon domains (contours). (a) Observations, and the group ensemble means of (b) LOW, (c) MED, and (d) HIGH.

protrudes all the way to northern Mexico, comparing quite well with the observations.

From the analysis of the climatological annual mean precipitation, we have shown the common biases that occurred in the tropical Pacific Ocean, such as the northeastward shift of the northern ITCZ and the unrealistic precipitation south of the equator. In addition to these errors, another common weakness in the simulations of seasonal rainfall is evident in the equatorial Atlantic Ocean. Figure 4 shows climatological summer- and wintertime precipitation over the tropical Atlantic Ocean derived from the GPCP and the GEMs. The observed Atlantic ITCZ is usually located at 5°–15°N during JJA (Fig. 4a) and at 0°–10°N during DJF (Fig. 4e). Because the Atlantic DJF ITCZ also stays north of the equator and near the equator, the observed AR has negative values of less than -2 mm day^{-1} in the equatorial North Atlantic Ocean, especially near 0°–5°N, as shown by the blue shading in Fig. 3a. The simulated Atlantic ITCZ during boreal summer appears to be reasonable in all GEMs, displaying comparable rainfall intensity and spatial patterns to the observations (Figs. 4b–d). On the other hand, the Atlantic DJF ITCZ in the models shows a wider rainband and tends to erroneously migrate to the south of the equator (Figs. 4f–h). As a consequence, all GEMs illustrate larger-than-observed AR in the equatorial North Atlantic Ocean between 0° and 5°N, as seen in Figs. 3b–d. A similar problem in the Community Climate System Model, version 3 (CCSM3), has been reported by Meehl et al. (2006). They found that the Atlantic DJF ITCZ and associated precipitation center produced by the CCSM3 lie mostly south of the equator. Our results, however, suggest that the unrealistic southward shift of the tropical Atlantic DJF ITCZ is not a particular CGCM problem, but likely a common weakness among the current coupled models.

4. Trend in global monsoon precipitation

a. Trend in continental monsoon region

Many studies devoted to the temporal changes of the regional monsoon precipitation over the last half a century have concluded there is a well-established increasing dryness at various monsoon regions (Nicholson 1993; Kripalani et al. 1996; Gong and Ho 2002; Chase et

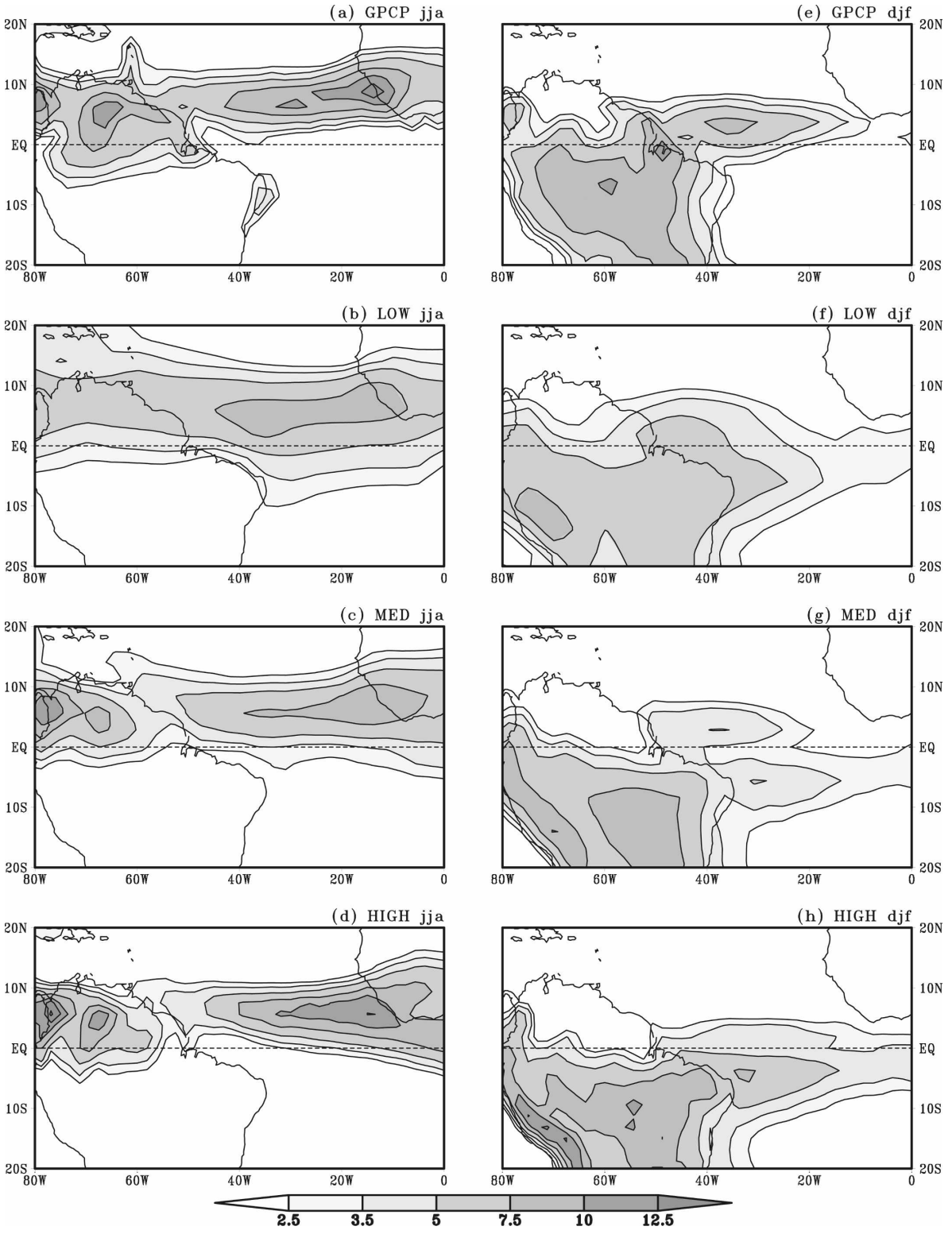

FIG. 4. Climatological seasonal precipitation (mm day^{-1}) during (left) JJA and (right) DJF over the tropical Atlantic Ocean obtained from the (from top to bottom) GPCP, LOW, MED, and HIGH. The data period is 1980–99.

al. 2003; Hoerling et al. 2006). In addition, the terrestrial rainfall has been altered considerably during the past 50 yr. The global continental precipitation, for instance, has undergone a drought tendency from the middle to the end of the twentieth century, though the centennial rainfall trend varied in sign (Boer et al. 2000). WD2006 also found out an overall decrease of the global land monsoon precipitation in the Northern Hemisphere during 1948–2003. Hence, it should be useful to examine a coherent spatial pattern of the land monsoon precipitation trend in the models. Toward this end, the primary spatial variability of the global land monsoon intensity for the period of 1951–99 is investigated.

Figure 5 presents the coherent pattern of the leading empirical orthogonal function (EOF) of yearly AR and its corresponding principal component [the annual range index (ARI)]. Here, the EOF analysis for the model simulations is carried out over the observed land monsoon domains. Given the observed spatial pattern that accounts for about 11% of the total variance (Fig. 5a), the corresponding ARI in Fig. 5e shows a declining tendency with a slope of -0.72 $(49\ \text{yr})^{-1}$. The Mann–Kendall rank statistics (Kendall 1955) and the trend-to-noise ratio indicate that the decreasing trend is significantly different from zero at the 99% confidence level (Table 2). Note, however, that the downward trend is evident mainly during the period from 1951 to the mid-1980s. The observed spatial pattern of the first EOF mode in association with the observed ARI depicts a prominent drying in the semiarid Sahel regions (Nicholson 1993; Le Barbé et al. 2002). Also seen is the weakening trend over southern Africa, which is confirmed by an analysis of station measurements (Hoerling et al. 2006). In addition, a moderately increasing aridity is found in parts of South Asia, though this trend depends on data period (Kripalani et al. 1996; Kripalani and Kulkarni 2001). Other regions that also experience a pronounced decreasing trend are northeastern China (Gong and Ho 2002; Yu et al. 2004) and central South America.

The leading EOF patterns and corresponding ARIs of the GEMs display intergroup differences. For the first EOF mode of the LOW group, which accounts for 10% of the total variance, its ARI shows a downward trend at the 95% confidence level (Figs. 5b,f, see also Table 2). However, the spatial pattern of the leading EOF mode depicts an opposite sign to the observations in most of the Northern Hemisphere land monsoon domains and central South America, indicating an unrealistic increasing tendency in monsoon rainfall in those regions. The leading eigenmode of the MED group explains about 9% of the total variance. The principal component of the MED shows no significant trend with a negligible negative slope (Table 2). This implies that the spatial pattern of the MED group accompanied by the corresponding ARI simply represents a short-term variability (Figs. 5c,g). The fractional variance explained by the first eigenvector of the HIGH group is about 7% of the total variance, the smallest among the GEMs. However, the ARI trend is more realistic with a decreasing tendency at a sufficient confidence level (Table 2). The spatial pattern and ARI of the HIGH group capture a rainfall decrease in the sub-Sahel regions and northern China as in the observations (Figs. 5d,h), although the enhanced wetness in South Africa and central South America is contrary to the observations.

It is important to note that the simulated EOF modes might not always match their corresponding observed counterparts. In the model simulation, the order of the modes could be interchanged, and one of the higher modes might correspond to the observed first EOF mode. For this reason, we further examined the second (EOF2) and third EOF (EOF3) modes of the observations and the GEMs (figure not shown). EOF2 and EOF3 in the observations account for about 8% and 6% of the total variance, respectively. Although the percentages of the total variance explained by these two eigenmodes are substantial when compared to the first EOF mode (EOF1; ~11%), the negative trends of the corresponding ARIs turn out to be statistically insignificant. The fractional variances of the next two modes in the GEMs are also nontrivial compared to their own EOF1, ranging from 6% to 8% for EOF2 (about 8% for the LOW group, 6% for the MED group, and 7% for the HIGH group) and from 6% to 7% for EOF3 (about 7% for the LOW group, 6% for the MED group, and 6% for the HIGH group). Again, however, the reproduced ARI trends in these modes are meaningless from the statistical standpoint. As such, it is arguable that EOF2 and EOF3 in the observations and the GEMs are all irrelevant for detection of the coherent drying pattern of the global land monsoon precipitation. One exception is that the third eigenmode of the HIGH group has a negative slope of -1.05 $(49\ \text{yr})^{-1}$ and its downward trend is significant at the 99% confidence level. However, unlike the leading EOF mode of the observations and the HIGH GEM, which delineates a more prominent aridity during 1951–85 (observations: -0.84 $(35\ \text{yr})^{-1}$ at the 99% confidence level, HIGH: -1.19 $(35\ \text{yr})^{-1}$ at the 95% confidence level), the downward trend of this particular mode is statistically insignificant for the first 35 yr. This

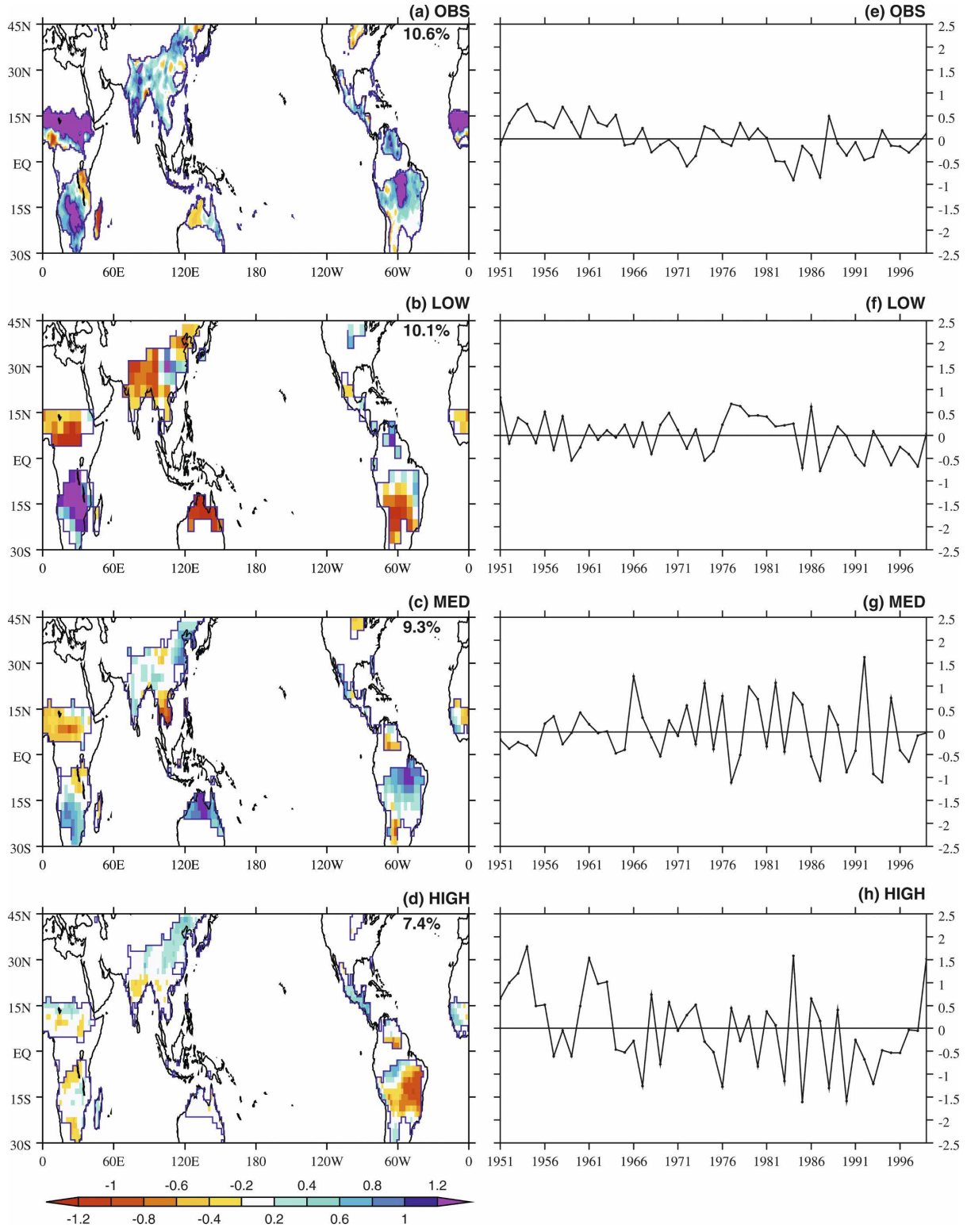

FIG. 5. (left) The spatial pattern of the EOF1 mode of the normalized annual precipitation range over the observed global land monsoon domain and (right) its corresponding principal component for the (from top to bottom) observations, LOW, MED, and HIGH. The numbers shown in the upper-right corners of left panels indicate the fractional variance explained by EOF1.

TABLE 2. Linear trends (1951–99) of the principal component of the EOF1 mode for the annual precipitation range over the observed global land monsoon domain. Statistical tests used are the Mann–Kendall rank statistics (MK) and the trend-to-noise ratio (T2N), and the linear trend is obtained by the least squares regression. Blank indicates the confidence level below 90%.

	Linear trend [ARI (49 yr)$^{-1}$]	Confidence level (%)	
		MK	T2N
OBS	−0.72	99	99
LOW	−0.44	95	95
MED	−0.06		
HIGH	−1.04	99	95

suggests that the EOF3 of the HIGH GEM is also inappropriate to the detection of the observed global land monsoon precipitation trend.

To investigate the global land monsoon rainfall trend in the models further, we also use the Northern Hemisphere land monsoon index (NHMI), defined as "*the JJA precipitation fallen into the Northern Hemisphere land monsoon domain*," which was used by WD2006 to show a significant declining tendency for the second half of the twentieth century. Figure 6 shows the time series of the NHMI for the observations and all individual model simulations over the period of 1951–99,

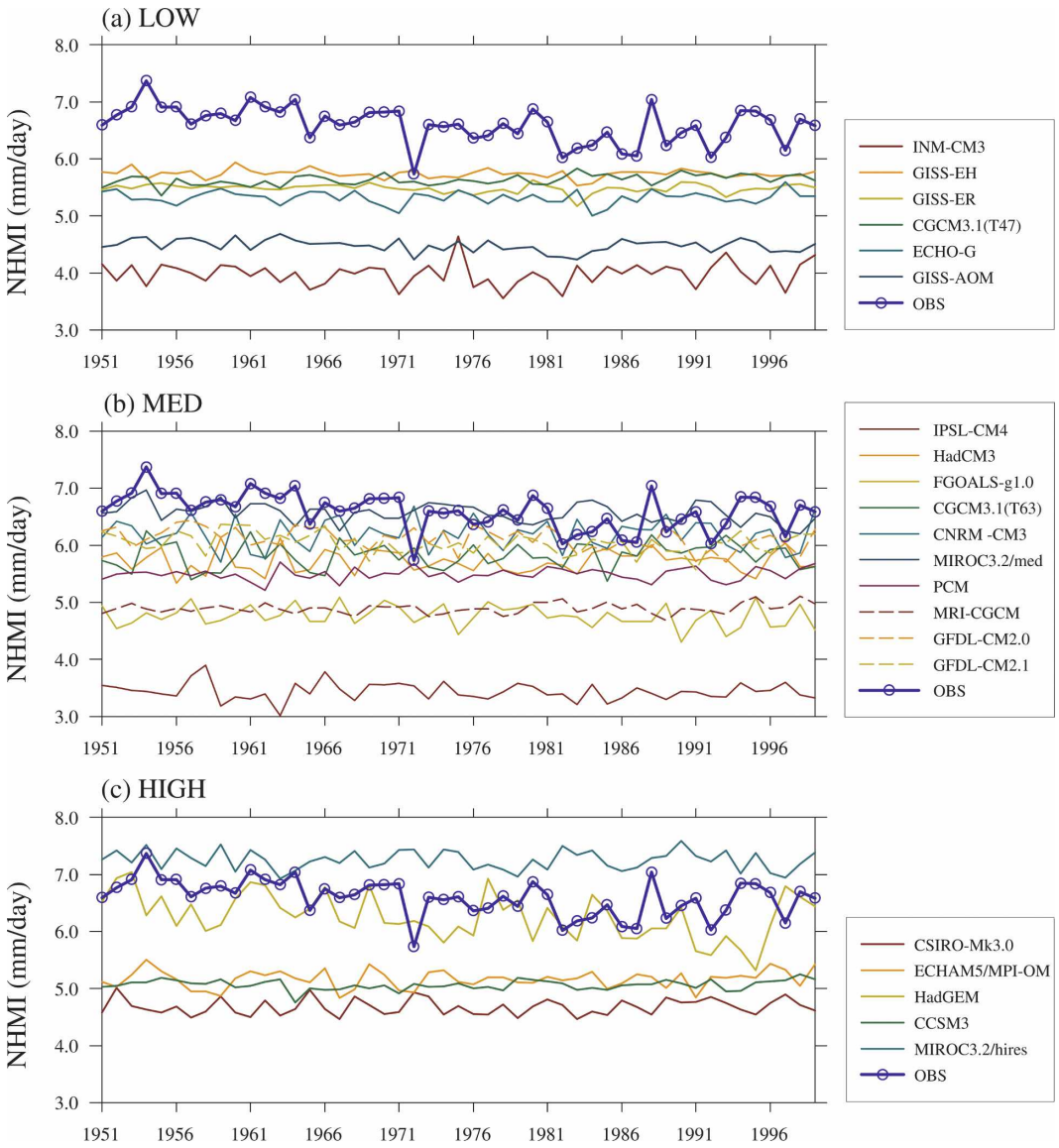

FIG. 6. Time series of the NHMI (mm day^{-1}). Members from the (a) LOW, (b) MED, and (c) HIGH groups over the period of 1951–99. Note that the observed land monsoon domain as shown in Fig. 5 is used to obtain the simulated NHMI.

TABLE 3. Linear trends of the simulated NHMI over the observed land monsoon domain obtained from the group ensemble means and individual model simulations. Statistical tests used are the MK and T2N, and the linear trend is obtained by the least squares regression; σ denotes a standard deviation, and blank indicates the confidence level below 80%.

	NHMI (1951–85)				NHMI (1951–99)			
			Confidence level				Confidence level	
Model	Trend [mm day^{-1} (35 yr)$^{-1}$]	$\frac{\sigma_{cgcm}}{\sigma_{obs}}$	MK	T2N	Trend [mm day^{-1} (49 yr)$^{-1}$]	$\frac{\sigma_{cgcm}}{\sigma_{obs}}$	MK	T2N
OBS	−0.62	—	99	99	−0.50	—	99	99
LOW	−0.10	0.17	99	99	−0.01	0.16		
MED	−0.05	0.17	80	90	−0.06	0.16	95	95
HIGH	−0.12	0.31	95	95	−0.10	0.31	95	95
INM-CM3.0	−0.12	0.66	80		0.03	0.63		
GISS-EH	−0.10	0.27	90	95	−0.05	0.23		
GISS-ER	−0.12	0.25	99	99	−0.05	0.24	80	
CGCM3.1 (T47)	0.11	0.29	90	95	0.15	0.28	99	99
ECHO-G	−0.12	0.38	80	90	−0.01	0.35		
GISS-AOM	−0.22	0.38	99	99	−0.11	0.33	95	95
IPSL CM4	−0.09	0.56			−0.07	0.48		
UKMO HadCM3	−0.03	0.64			0.02	0.59		
FGOALS-g1.0	0.02	0.52			−0.13	0.58		80
CGCM3.1 (T63)	0.01	0.76			0.11	0.69		
CNRM-CM3	−0.03	0.83			−0.01	0.79		
MIROC3.2(medres)	−0.10	0.50			−0.22	0.52	95	99
PCM	0.07	0.32	80		0.05	0.33		
MRI CGCM2.3.2a	0.04	0.25			0.06	0.28		80
GFDL CM2.0	−0.20	0.54	90	95	−0.27	0.57	99	99
GFDL CM2.1	−0.21	0.55	95	95	−0.17	0.55	90	95
CSIRO Mk3.0	−0.07	0.48			0.04	0.44		
ECHAM5/MPI-OM	−0.01	0.51			0.06	0.49		
UKMO HadGEM1	−0.42	1.10	95	95	−0.58	1.21	99	99
CCSM3	−0.05	0.27	80		0.03	0.27		
MIROC3.2(hires)	−0.06	0.53			−0.07	0.53		

where the observed land monsoon domain is used to derive the NHMI in the models (see Fig. 5 for the observed land monsoon domain for each group). The observed time series delineates a conspicuous decreasing trend during the whole period, particularly before the mid-1980s. The linear trend is −0.50 mm day^{-1} (49 yr)$^{-1}$ for the entire 49 yr and −0.62 mm day^{-1} (35 yr)$^{-1}$ for 1951–85, respectively. The Mann–Kendall rank statistics and the trend-to-noise ratio indicate that both trends are significant at the 99% confidence level (Table 3).

The simulated time series in Fig. 6 displays some intriguing features in terms of interannual variability and intensity of the NHMI. The yearly variations are generally suppressed not only in the models with multiple realizations due to the averaging process that filters out much of the year-to-year variability, but also in those with a single realization. As a result, for all but the Met Office (UKMO) Hadley Centre Global Environmental Model, version 1 (HadGEM1), the standard deviation of the NHMI time series is quite small when compared to that of the observations (Table 3). Moreover, the strength of the NHMI is much weaker in most CGCMs, with the exception of the Model for Interdisciplinary Research on Climate 3.2, high-resolution version [MIROC3.2(hires)] that overestimates the observed NHMI intensity. Note that the robust underprediction of the simulated monsoon precipitation is found only over the Northern Hemisphere land monsoon domain. The underestimation of the NHMI among the models is about 18%, on average. In contrast, the intensity of the modeled Southern Hemisphere monsoon index (SHMI), denoted by *the DJF precipitation fallen into the Southern Hemisphere land monsoon domain,* is almost as strong as that observed in the majority of the CGCMs (figure not shown). Further, the oceanic monsoon precipitation in the models is generally stronger than that in the observations (see Fig. 7). The multimodel ensemble mean intensities of the SHMI and oceanic monsoon precipitation are overestimated by about 2% and 7%, respectively.

The modeled NHMI trends during 1951–85 and 1951–99 and their confidence levels obtained from individual model simulation are provided in Table 3. Most models produce a negative slope of the NHMI over the first 35-yr period and about half of the models

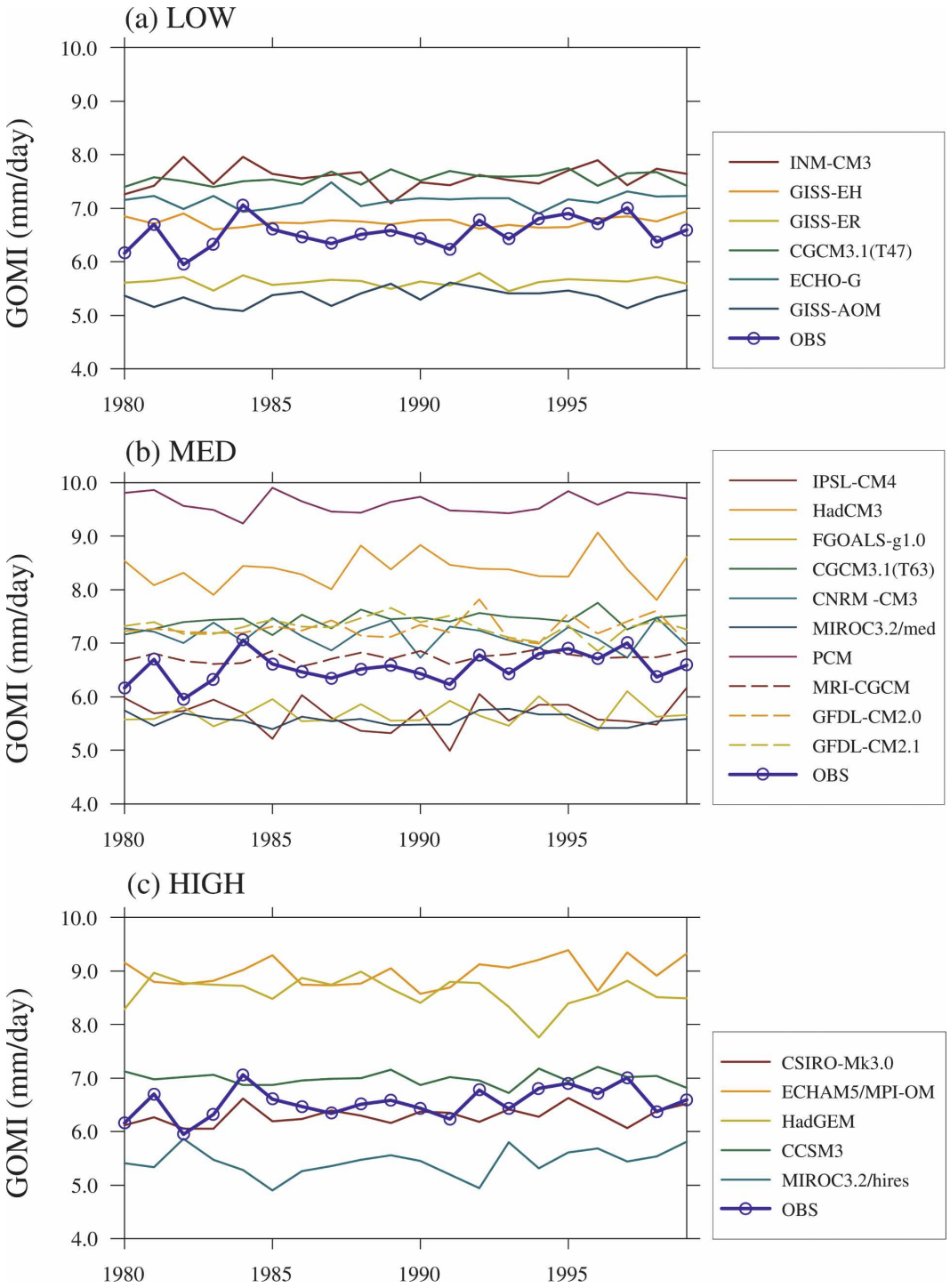

FIG. 7. Time series of the GOMI (mm day^{-1}). Members from the (a) LOW, (b) MED, and (c) HIGH groups over the period of 1980–99. Note that the observed ocean monsoon domain as shown in Fig. 3a is used to obtain the simulated GOMI.

portray a downward trend over the entire period, although the negative slopes in the models tend to be weaker than that of the observations, except for the UKMO HadGEM1. As a consequence, the simulated decreasing trends are generally statistically insignificant; only 7 (5) models out of 21 exhibit the weakening trend with a confidence level higher than 80% for the period of 1951–85 (1951–99). However, it is worth not-

ing that the models with the significant declining NHMI trend take into account the volcanic aerosols except for Goddard Institute for Space Studies Atmosphere–Ocean Model (GISS-AOM; also see Table 1).

In the HIGH GEM, the trend and interannual variability of the NHMI seem to be reproduced better when compared to the other GEMs. The HIGH GEM shows the largest year-to-year variation and negative trends with a sufficient confidence level (Table 3). Moreover, only the leading EOF mode of the HIGH GEM is able to depict the observed increasing aridity in the sub-Sahel regions and northern China as discussed earlier in this section. Do these improvements in the HIGH GEM reflect the advantage of the finer resolution in simulating the long-term variations of the global land monsoon precipitation? To address this question, a new HIGH GEM is performed, excluding the UKMO HadGEM1's outputs because in the HIGH group, the UKMO HadGEM1 is the only model that has the significant drying trend with the largest negative slope for both periods (Table 3). The result from this alternative GEM shows that the NHMI trend is insignificant both for the first 35 yr and the entire period, and the spatial pattern of the first EOF mode changes sign over the sub-Sahel regions with a statistically meaningless ARI trend (figure not shown). This suggests that the improvement in the HIGH group may not be attributed to a common amelioration across its members resulting from a refined resolution but likely to a prevailing influence of the UKMO HadGEM1 on the overall trend of the HIGH GEM.

TABLE 4. Same as Table 3, but for the observed and simulated GOMI for the period of 1980–99. Note that the simulated GOMI is obtained over the observed ocean monsoon domain.

	GOMI (1980–99)			
			Confidence level	
Model	Trend [mm day^{-1} (20 yr)$^{-1}$]	$\frac{\sigma_{cgcm}}{\sigma_{obs}}$	MK	T2N
OBS	0.37	—	90*	90
LOW	0.09	0.19	95	95
MED	0.04	0.19		
HIGH	0.08	0.26		80
INM-CM3.0	0.08	0.77		
GISS-EH	0.04	0.32		
GISS-ER	0.02	0.31		
CGCM3.1 (T47)	0.13	0.40	90	80
ECHO-G	0.09	0.47	80	
GISS-AOM	0.17	0.53	80	80
IPSL CM4	−0.03	1.07		
UKMO HadCM3	0.17	1.08		
FGOALS-g1.0	0.08	0.71		
CGCM3.1 (T63)	0.23	0.53	95	95
CNRM-CM3	−0.17	0.81		
MIROC3.2 (medres)	−0.04	0.42		
PCM	0.05	0.64		
MRI CGCM2.3.2a	0.12	0.34	80	90
GFDL CM2.0	0.10	0.72		
GFDL CM2.1	−0.12	0.63		
CSIRO Mk3.0	0.23	0.60	95	90
ECHAM5/MPI-OM	0.28	0.92		80
UKMO HadGEM1	−0.30	1.01		80
CCSM3	−0.02	0.43		
MIROC3.2 (hires)	0.23	0.90	80	

* Rounded off from a confidence level of 89.5%.

b. *Oceanic monsoon precipitation trend*

Global mean temperature has shown the most rapid increase since 1980 (e.g., Waple et al. 2002). To simulate this warming in a CGCM, all experiments are carried out with the historical variation of greenhouse gases, which in fact results in an increasing tropospheric warming in the models (Hegerl et al. 2007). Because this warmer condition most likely favors more abundant water vapor in the model troposphere, thereby intensifying precipitation, tracking the increasing aridity in the global land monsoon precipitation could be difficult. Indeed, the observed oceanic monsoon precipitation has shown an increasing wetness after 1980 in concert with the rapid global warming (WD2006). Then, what about the simulation of the upward rainfall trend in the models? Figure 7 gives the time series of the global ocean monsoon index (GOMI), defined by "*the local summer precipitation fallen into the global oceanic monsoon domain*" during the period of 1980–99. Here, we have also used the observed ocean monsoon domain shown in Fig. 3a to obtain model GOMI. The observed GOMI depicts an increasing wetness with a slope of 0.37 mm day^{-1} (20 yr)$^{-1}$. The same statistical tests show that the recent increasing trend over the global ocean monsoon domain is significantly different from zero at the 90% confidence level (Table 4). In comparison with the observations, the models with the excessive GOMI considerably outnumber those with the underestimated GOMI (Fig. 7). This is quite different from the modeled NHMIs that have illustrated the less-than-observed NHMI in almost all models (Fig. 6). However, the simulated interannual variability of the individual GOMI is generally weaker than the observed (Table 4), as is the NHMI.

The trends and significance tests for the simulated GOMI are summarized in Table 4. Most CGCMs are able to capture a positive trend of the time series in terms of the simulated GOMI. Again, however, these trends are generally statistically insignificant; only five models show significant increases at a confidence level higher than 80%. Nevertheless, it is interesting to note

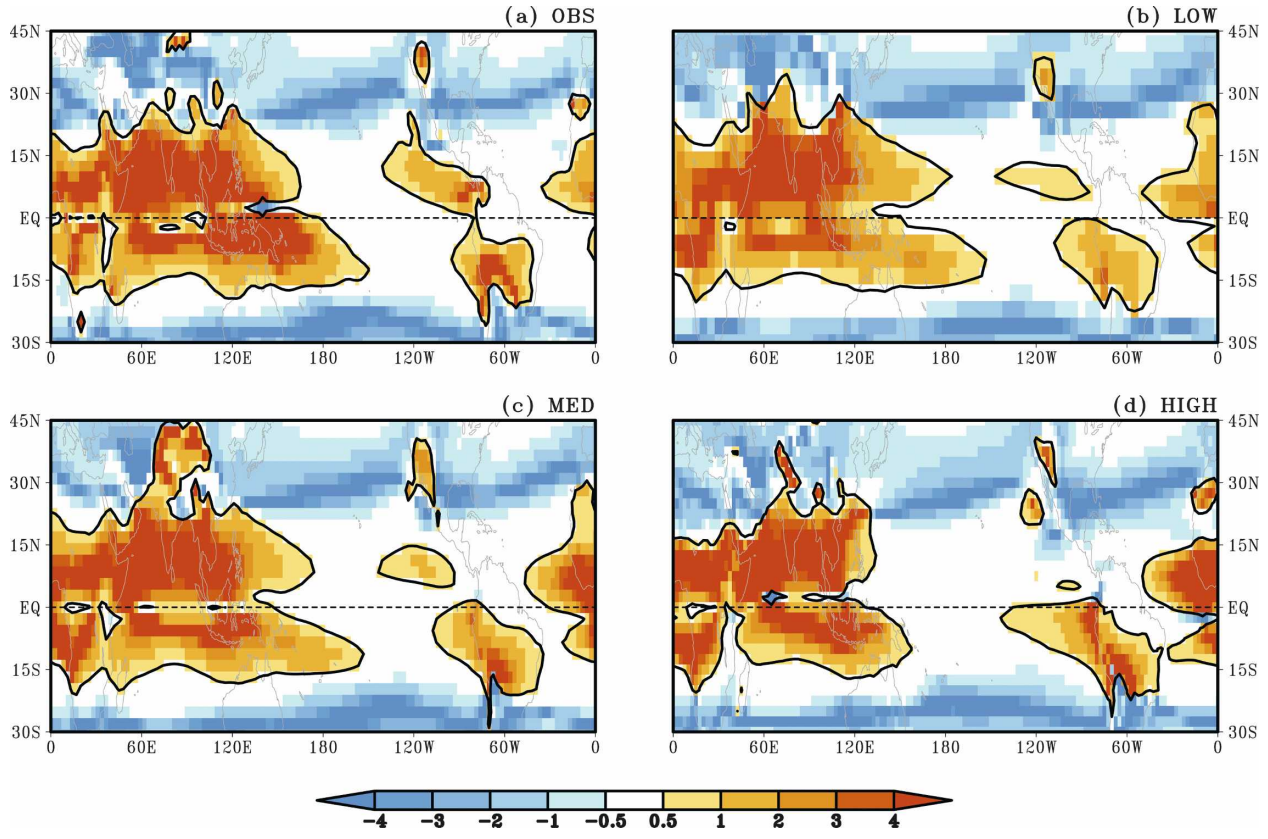

FIG. 8. Climatological MWI (shading) and the monsoon westerly domains (contours). (a) Observations, and the group ensemble means of the (b) LOW, (c) MED, and (d) HIGH groups.

that the significant positive GOMI trend occurs in the models that are free of volcanic aerosols except for Meteorological Research Institute Coupled General Circulation Model, version 2.3.2a (MRI CGCM2.3.2a; see Table 1). This, along with the fact that the significant drying NHMI trend is seen mainly in the models with volcanic aerosols, indicates that the natural volcanic forcings could be an important contributor in simulating the global monsoon precipitation. Therefore, we further investigated the sensitivity of the modeled trend to the inclusion of the volcanic aerosols and the results will be presented in section 6.

5. Global monsoon circulation

The global monsoon can be also characterized by the seasonal reversal of the prevailing winds. In fact, the term "monsoon" originally stems from the seasonal variations in winds, and it is surface winds that have been traditionally used to define monsoon (Ramage 1971). More recently, Wang and Ding (2008) introduced a monsoon westerly index (MWI) defined by the ratio of annual range[2] to the annual mean wind speed of 850-hPa zonal winds. They demonstrated that the global monsoon westerly domains delimited by MWI greater than 0.5 are dynamically consistent with the global monsoon precipitation domains. In this section, we examine the realism of the simulations of the climatological global monsoon westerly domain by applying the methodology of Wang and Ding (2008). We then compare the modeled trend of the global monsoon circulation with that observed.

The global monsoon westerly domains for the observations and the GEMs are presented in Fig. 8. All GEMs are in good agreement with the observations in demarcating the monsoon westerly domains around the globe. The pattern correlation coefficient (PCC) for the annual range of 850-hPa zonal winds between the observations and the GEMs weighted by cosine of latitude

[2] The annual range for MWI is based on the extended local summer and winter that consist of May–September (November–March) and November–March (May–September) for the Northern Hemisphere (Southern Hemisphere), respectively.

TABLE 5. Linear trend of the principal component for the annual westerly range that is significant among the first three EOF modes. The observed global monsoon westerly domains shown in Fig. 8a are applied in common to the model simulations. Statistical tests used are the MK and T2N, and linear trend is obtained by the least squares regression. The fraction of variances (%) shown in the first column are for the period of 1951–99.

	1951–85			1951–99		
	Linear trend $(35\ \text{yr})^{-1}$	Confidence level (%)		Linear trend $(49\ \text{yr})^{-1}$	Confidence level (%)	
		MK	T2N		MK	T2N
OBS (EOF2: 9.0%)	−3.39	99	99	−3.06	99	99
GISS-AOM (EOF2: 8.3%)	−0.81	95	95	−0.57	95	95
UKMO HadGEM1 (EOF1: 12.5%)	−1.27	90	90	−1.93	95	99

is almost similar (~0.94) among the GEMs. The observed dominant monsoon westerly domains include the Asian, Australian, African, and South American monsoons, as well as the North American monsoon, which is primarily located over the eastern North Pacific, as documented by Murakami et al. (1992). It is well known that the tropical monsoon circulation is intimately related to the monsoon precipitation, which, through latent heat release, plays a central role in driving tropical circulation. A Rossby wave response to the precipitation heat source is expected to favor the monsoon westerly domains residing at the equatorward and westward sides of the monsoon precipitation domains. This physical constraint seems to be generally valid both in the observations and model results (Figs. 3 and 8).

For the purpose of probing the trend of the global monsoon circulation, we repeated the EOF analysis for the observations and all individual model solutions over the observed westerly monsoon domains. In the observations, the time series of the second EOF mode among the first three eigenmodes displays a significant weakening over the period of 1951–85 $[-3.39\ (35\ \text{yr})^{-1}]$ and 1951–99 $[-3.06\ (49\ \text{yr})^{-1}]$, as shown in Table 5. Note that the former is more pronounced than the 49-yr trend similar to that revealed in the observed precipitation tendency. Figures 9a,d present the spatial pattern and corresponding principal component of this mode. It is important to point out that the time series in Fig. 9d appears to be quite similar to that in Fig. 5e; the correlation coefficient between these two time series is about 0.64. The observed spatial pattern of the second EOF mode along with the corresponding principal component indicates a reduction of low-level monsoon flows chiefly in the North African and South Asian monsoon regions during the last 49 yr, which is consistent with the observed downward trend of the land monsoon precipitation over those regions. The strengthened monsoonal circulations found in the tropical western Pacific Ocean, however, must be treated with caution because the enhanced oceanic monsoon rainfall is measured only for the recent 20 yr, not for the entire period used for the EOF analysis.

The models with annual westerly range trends that are significant both over 1951–85 and 1951–99 are listed in Table 5. Here, we have tested the significance of linear trends of the principal components up to the first three EOF modes using all individual model results. In view of the skill-less aspect of the models in reproducing the observed monsoon rainfall trend, it is expected that many models might fail to capture the negative trend seen in the observations with a sufficient confidence level. Indeed, only two models (GISS-AOM and UKMO HadGEM1) can replicate the decreasing trend in the observations. Furthermore, though the simulations of the GISS-AOM delineate the diminished monsoonal circulations in the African Sahel and the South Asian regions relatively well (Figs. 9b,e), the results of the UKMO HadGEM1 show no skills in modeling the reduction of the low-level flows in those regions (Figs. 9c,f). Accordingly, we conclude again that the detection of the multidecadal changes in the global monsoon circulations by using the present-day climate models is difficult and the models with finer resolution do not provide better representation in tropical monsoon circulation trend.

6. Effects of volcanic forcing on the simulations of the global monsoon rainfall trend

Previous studies have demonstrated that the simulated land mean precipitation in the CMIP3 climate model integrations forced by both natural and anthropogenic forcings is significantly correlated with that observed, thus identifying some external influences on the observational precipitation (e.g., Lambert et al. 2005). In particular, the external forcing resulting from volcanic aerosols has proven to be a key player not only in simulating multidecadal variability of the global land precipitation in climate models (Broccoli et al. 2003;

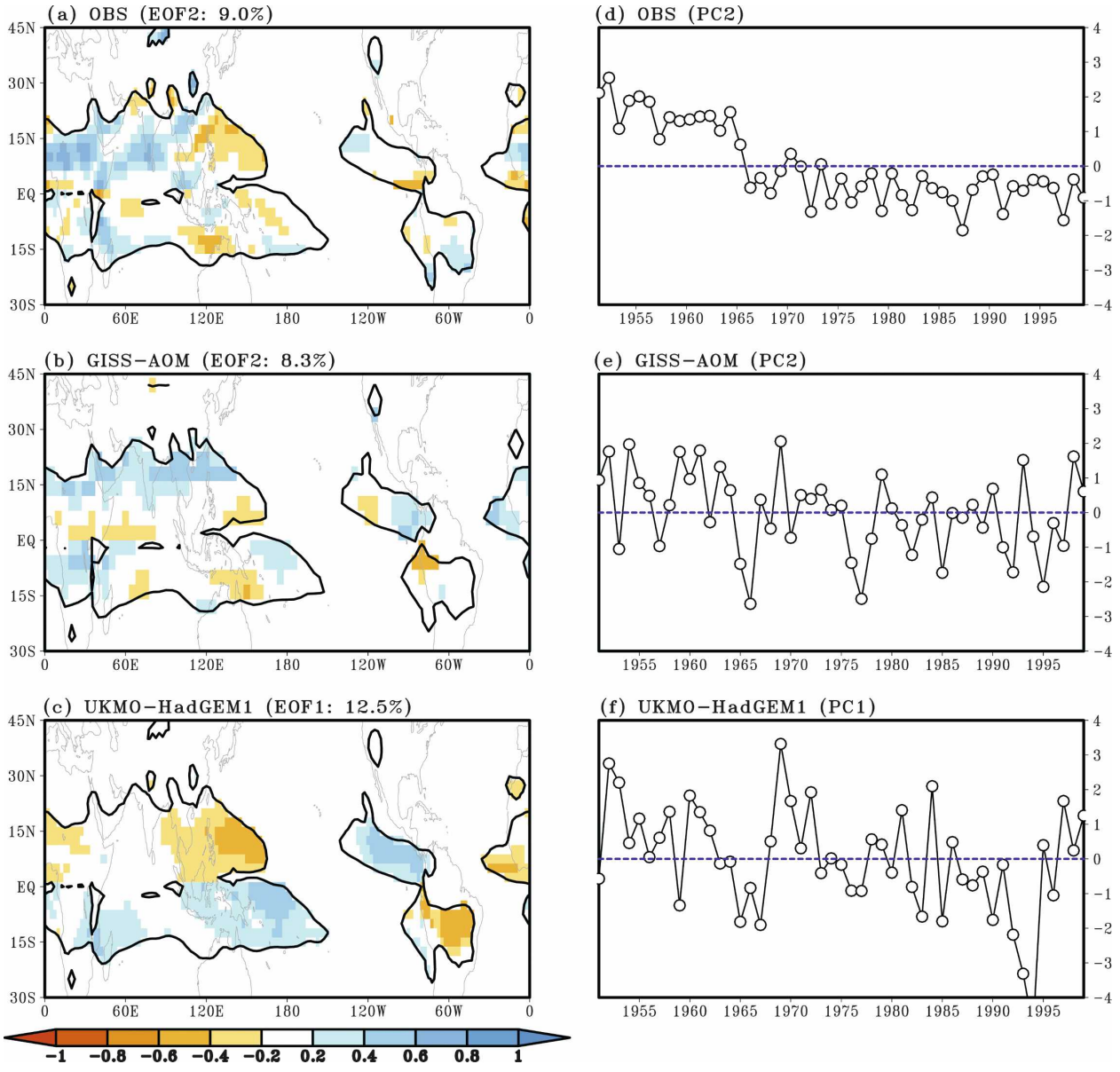

FIG. 9. (left) The spatial pattern of EOF mode of the normalized annual westerly range and (right) its corresponding principal component for the (top) observations, (middle) GISS-AOM, and (bottom) UKMO HadGEM1.

Gillett et al. 2004), but also in attributing changes in the observed terrestrial rainfall over the past 50 yr (Gillett et al. 2004; Lambert et al. 2005). Our results presented in section 4 also suggest the climatic importance of the natural volcanic forcings in the simulated global monsoon precipitation. In this section, therefore, we will discuss the response of the global monsoon precipitation to the natural volcanic forcing in the CMIP3 models.

The 21 CGCMs were partitioned into two sets—with and without volcanic aerosols (VOL and No-VOL, respectively, as shown in Table 1)—based on Phillips and Gleckler (2006). Phillips and Gleckler (2006) provided a comprehensive description of the external forcings used in the CMIP3 models and the specification of the volcanic aerosols in their study agrees well with others (e.g., Santer et al. 2005, 2006).

Figure 10 shows the scatter diagram indicating the relationship between the modeled global monsoon precipitation trend and volcanic forcings. Most of the VOL models (solid circles) tend to have a negative NHMI trend for the 1951–99 period, while more than half of

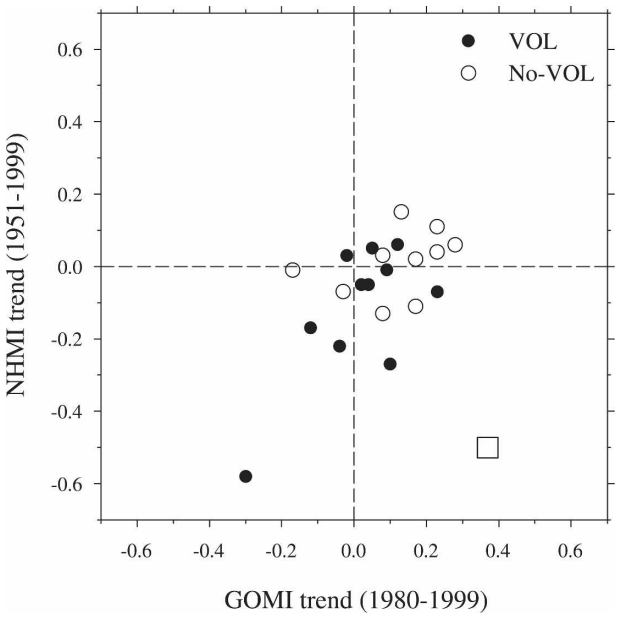

FIG. 10. Scatter diagram of the trends between the global oceanic monsoon rainfall and Northern Hemisphere land monsoon precipitation [mm day^{-1} (20 yr)$^{-1}$ for ocean trend and mm day^{-1} (49 yr)$^{-1}$ for land trend]. Solid (open) circles are for the models with (without) historic volcanic forcing and hollow squares denote the observations.

the No-VOL models (open circles) depict an increasing rainfall over the Northern Hemisphere land monsoon regions. The trends between VOL and No-VOL are statistically different at a confidence level higher than 90% using the *t* test. This test was also performed without the UKMO HadGEM1 in VOL (the solid circle shown at the lower-left corner in Fig. 10) and results in the same statement with a confidence level of about 90% (89.4%). Stratospheric aerosol experienced an abrupt increase since the 1960s because of the abnormally large eruptions after the 1960s. Although the magnitude of volcanic forcing differs among the reconstructions used in the CMIP3 models, the timing and duration of the volcanic eruptions are well documented (Sato et al. 1993; Ramachandran et al. 2000; Hansen and Sato 2001; Ammann et al. 2003). Therefore, the more robust downward trend in VOL than in No-VOL could be suggestive of the impact of volcanic forcing that likely leads to a reduction in the simulated land monsoon precipitation over the Northern Hemisphere.

However, a question arises as to whether the different aspects of the NHMI trend between the VOL and No-VOL models stand out against the internal variability of each model or whether they occur because of chance. To answer this question, we analyzed the preindustrial control integrations (PI) in which all external climate forcings remain invariant in time; thereby, variability can be considered a representation of the pure natural noise of the climate system. By comparing the results from the PI and 20C3M simulations, Biasutti and Giannini (2006) determine the significance of the modeled Sahel rainfall response to the twentieth-century forcings against the internal variability of each model and evaluated the externally forced component of the Sahel drought. In this study, we adopted their methodology to examine the significance of the volcanic forcings in replicating the global monsoon trend.

Figure 11 shows the 49-yr NHMI trend difference between the 20C3M (1951–99) and PI simulations. Here, the average of the sliding NHMI trends with a 49-yr window is used to represent the 49-yr NHMI trend in the PI integrations. Figure 11 also depicts the range of natural variability in the 49-yr NHMI trend of each PI simulation expressed by one and two standard deviation limits. If the magnitude of the NHMI trend difference is greater than one standard deviation, the corresponding 20C3M NHMI trend can be considered significant against the internal variability. It is seen in Fig. 11 that except for four models [ECHAM and the global Hamburg Ocean Primitive Equation (ECHO-G), Parallel Climate Model (PCM), UKMO Third Hadley Centre Coupled Ocean–Atmosphere General Circulation Model (HadCM3), and Centre National de Recherches Météorologiques Coupled Global Climate Model, version 3 (CNRM-CM3)], the NHMI trend difference is significant or at least marginally significant. This suggests that the twentieth-century forcings are, in general, responsible for the 49-yr NHMI trend detected in the 20C3M integrations. Specifically, the difference is substantially negative in 7 models out of 11 VOL models, although MIROC3.2(hires) is marginal (Fig. 11a). Meanwhile, the negative difference is significant only in a minority of the No-VOL models; one-half of the No-VOL models show positive NHMI trend difference beyond or very close to one standard deviation (Fig. 11b). These results indicate that the contrasting features of the 20C3M NHMI trend identified between the VOL and No-VOL models could be, at least in part, ascribable to the inclusion of the external volcanic forcings.

On the other hand, the volcanic aerosols seem to little affect the oceanic monsoon rainfall trend because most of the VOL and No-VOL models have an upward oceanic monsoon precipitation trend (Fig. 10). Is the GOMI trend insensitive to the inclusion of the volcanic eruptions? Figure 12 shows the 20-yr GOMI trend difference between the 20C3M (1980–99) and the PI simulations. In most VOL models, the positive GOMI trend is in the range of internal variability of each model (Fig. 12a). This may be caused either by chance or (more

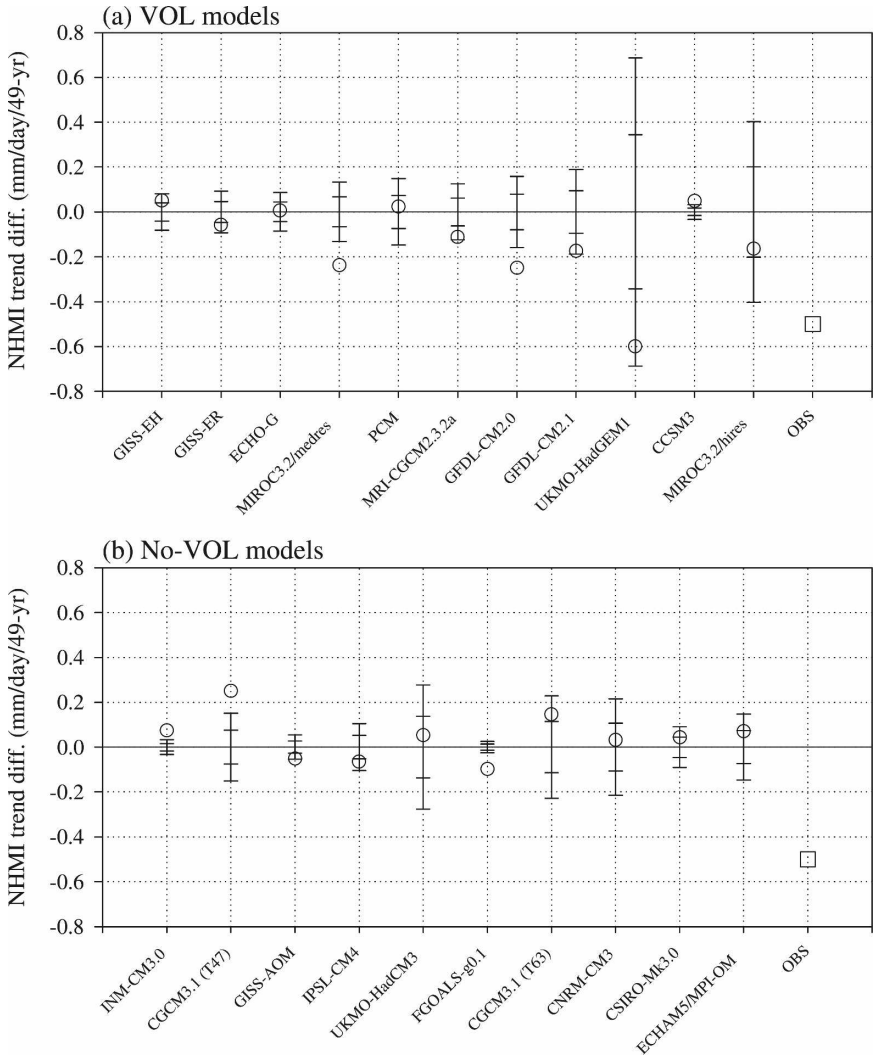

FIG. 11. The 49-yr NHMI trend difference between the 20C3M (1951–99) and the PI simulations. The 49-yr NHMI trend in the PI integrations is derived from the average of the sliding NHMI trends with a window of 49 yr. Vertical bars indicate one and two standard deviations in the 49-yr PI NHMI trend and square denotes the observed NHMI trend.

likely) by the shortwave cooling of volcanic aerosols that compensate for the ocean warming resulting from greenhouse gases and eventually weakens an increasing GOMI trend. In contrast, nearly half of the No-VOL models show a significantly positive GOMI trend (Fig. 12b). Therefore, it is argued that the positive GOMI trend in the 20C3M simulations is also influenced by the volcanic forcings to some extent. The increasing trend becomes more significant in No-VOL than in VOL. It is also of interest to note that in no case, except for CNRM-CM3, is the GOMI trend difference significantly negative. This implies that regardless of the external forcings specified for the 20C3M simulations, the model response to the twentieth-century forcings would not favor a drying tendency in the global oceanic monsoon precipitation over the past 20 yr.

7. Conclusions and discussion

CGCMs have been widely utilized to build up our knowledge and understanding of how components of the earth's climate system are interlinked and how they will evolve, especially due to increasing greenhouse gases and changing natural forcings. However, unlike a hindcast study, CGCM predictions of climate change cannot be verified until the projected climate state comes into existence. Therefore, it is generally accepted that the credibility of a CGCM's predictions of regional

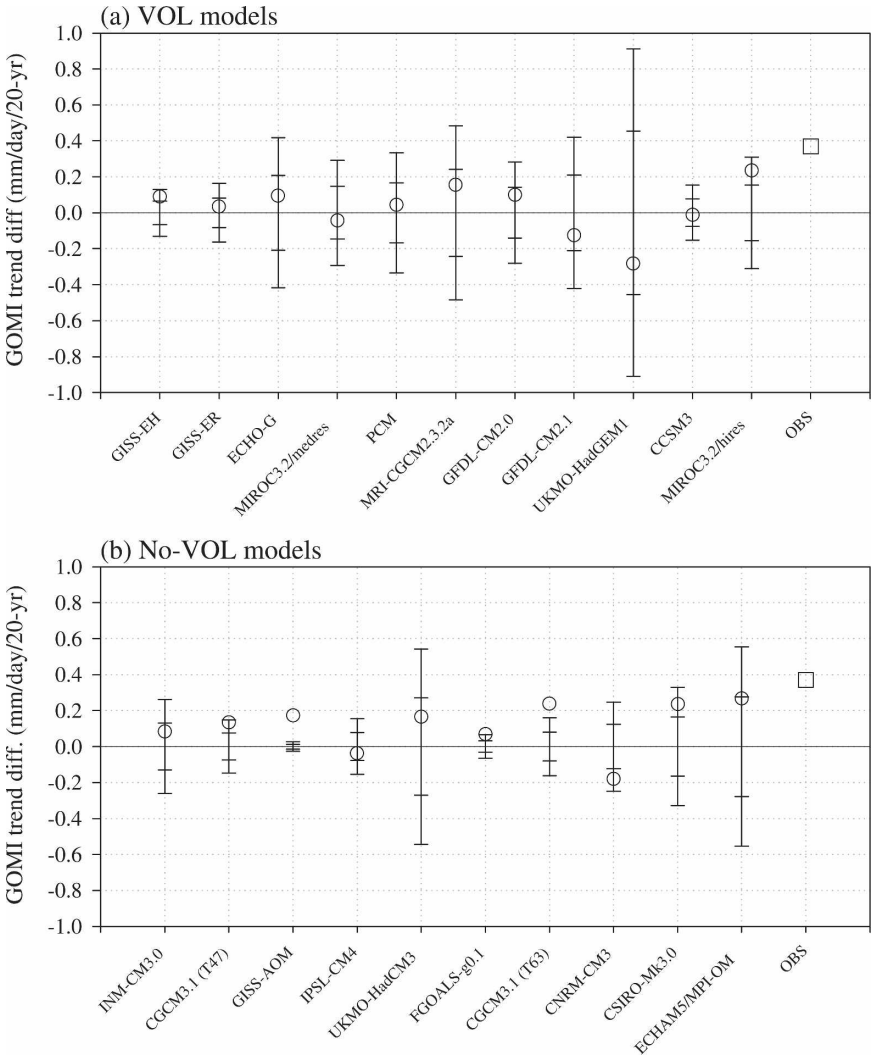

FIG. 12. Same as Fig. 11, but for the GOMI trend for the period of 1980–99.

and global climate changes relies upon the model's capability in simulating present-day conditions. In this respect, the authors have evaluated the WCRP's CMIP3 multimodel dataset for the twentieth-century simulations to document current status of cutting-edge CGCMs. With the 65 realizations (20 realizations for zonal winds) for the period of 1950–99 collected from 21 CGCMs, the present study casts light on the realism of the climatological global monsoon simulations, the long-term trend of the simulated global monsoon precipitation and circulation, and the response of the reproduced monsoon precipitation to volcanic forcing, as well as the dependence of the model monsoon rainfall and flows on the atmospheric model's horizontal resolution.

In contrast to the greater number of studies that have evaluated the reality of the simulated temperature trend, relatively few studies have focused on the modeled precipitation trend, and the climate models used in such study are very limited. Therefore, the results presented herein are of value to a growing body of climate modeling studies that address multidecadal rainfall variability in global monsoon climate.

a. Conclusions

All GEMs (group ensemble means obtained from the three different resolution groups) are able to reproduce the major aspects of the observed spatial pattern of the climatological annual mean precipitation. The PCC between the observations and the GEMs is about 0.82, 0.85, and 0.85 for the LOW, MED and HIGH groups, respectively. However, the fictitious ITCZ precipitation band south of the equator over the central and eastern Pacific is still an unsolved problem in most CGCMs. In

addition, a slight northeastward shift of the ITCZ is found to be common in the tropical North Pacific. We also notice that the modeled rainbelt associated with the Atlantic ITCZ tends to broaden because of its spurious southward migration during boreal winter, which results in a larger-than-observed annual cycle in precipitation at the equatorial North Atlantic Ocean.

Following WD2006, climatological annual range of precipitation and the ratio of summer to annual precipitation in conjunction with a couple of objective criteria are used to define global monsoon precipitation domain. All GEMs can capture the major monsoon rainfall regions around the globe. However, regional aspects of monsoon rainfall simulations show remarkable differences depending on atmospheric models' horizontal resolutions. As the resolution increases, the model topography is better resolved and various monsoon regimes affected by mesoscale terrains show improved details in the GEM simulations of the monsoon demarcation, especially along the steep slope of the Tibetan Plateau and western coast of Mexico. The spatial pattern of the GEM annual range over the Asian regions, where orographic lifting plays a key role in determining monsoon precipitation, also displays a positive impact of the refined horizontal resolution; the PCC of the annual range between the observations and each GEM calculated over the Asia region (Asia monsoon region)[3] is increased from 0.75 (0.55) for the LOW group to 0.80 (0.56) for the MED group, and to 0.82 (0.66) for the HIGH group.

The local summer rainfall fallen into the Northern Hemisphere land monsoon domain is underestimated in all models except for MIROC3.2(hires), while that over the Southern Hemisphere land monsoon domain is usually similar to that observed. Even the monsoon precipitation over the global ocean is rather overestimated in the majority of the model.

Unlike the positive effect of the increased resolution in modeling regional precipitation climatology, the model resolution does not show a considerable influence on the multidecadal trend simulations. However, the trend in the global monsoon precipitation detected in the CMIP3 models is generally consistent with the observations, albeit with much weaker magnitude. Statistical tests reveal that 5–7 (5) models out of 21 can replicate the observed NHMI (GOMI) trend with an acceptable confidence level. Interestingly, the significant decreasing NHMI trend occurs mainly in the models with volcanic aerosols and the significant positive GOMI trend appears chiefly in those without volcanic aerosols. Furthermore, while most models simulate a downward NHMI trend for the period of 1951–85, the negative slope is produced mostly in the VOL models during 1951–99, the period where a recent rapid rise of the radiative forcing from the increasing greenhouses gases is specified across the models so that the inclusion of the volcanic aerosols could be more discernable than in the first 35-yr period. Indeed, the different behavior in the 49-yr NHMI trend between VOL and No-VOL turns out to be significant at a confidence level higher than 90% using the *t* test.

Analyses have been extended to the significance of the natural volcanic forcing in simulating the global monsoon trend against the internal variability of each model. About half of the No-VOL models exhibit a significantly positive 20C3M–PI difference in the 49-yr NHMI trend and in the 20-yr GOMI trend. In most of the VOL models, in contrast, the difference becomes significantly negative for the NHMI trend or indistinguishable from the internal variability in the GOMI trend.

We proposed that the volcanic forcings play an important role in reproducing the global monsoon precipitation trend and could result in a considerable reduction in the Northern Hemisphere land monsoon precipitation. Following the approach of Biasutti and Giannini (2006), we made a rough estimate for the influence of the volcanic forcings on the 49-yr NHMI trend by comparing the 20C3M–PI difference in VOL and No-VOL with the observed NHMI trend. The observed trend [-0.5 mm day^{-1} (49 yr)$^{-1}$, see Table 3] corresponds to about 8% decrease in the Northern Hemisphere land monsoon precipitation over the period of 1951–99. The 20C3M–PI difference in the VOL models is, on average, -0.13 mm day^{-1} (49 yr)$^{-1}$, which accounts for 26% of the observed NHMI trend, but that in the No-VOL models is slightly positive, with a value of 0.05 mm day^{-1} (49 yr)$^{-1}$. We conclude that from about one-fourth to one-third of the drying trend in the Northern Hemisphere land monsoon precipitation over the latter half of the twentieth century was likely forced by the volcanic aerosols.

b. Discussion

The impact of improved resolution on the model simulations (e.g., monsoon precipitation simulations) is examined typically by conducting a sensitivity test using a single model (e.g., Meehl et al. 2006). The core physical processes related to rainfall simulations are convection and gridscale precipitation parameterizations. The CMIP3 models all employ these parameterizations, but the schemes used differ widely across the models. In

[3] The Asia region indicates the area of 0°–30°N, 60°–130°E, and the Asia monsoon region refers to the monsoon domain in this area.

addition, none of the precipitation schemes are known to be superior to the others in every region and on every time scale. This suggests that internal variability in model-simulated precipitation is uncorrelated among the ensemble members of a group. Therefore, it is reasonable to consider that better rainfall simulations in a particular region (i.e., near the narrow mountains) produced in a GEM do not result from a coincidental superiority in representing precipitation parameterization among the models in a group but from a common factor shared across the members of it, that is, the improved horizontal resolution.

The volcanic signal in the simulated 49-yr NHMI trend is, in general, detectable against the internal variability of each model, and the sign of the trend varies significantly with the inclusion of the volcanic forcings. These results provide useful information relevant to climate modeling study. Using the UKMO HadCM3, Lambert et al. (2004) argued that variation in terrestrial precipitation is controlled more by the natural shortwave forcing of volcanic aerosols than by the longwave forcing of greenhouse gases. Our results, lending support to their speculation, confirm an essential role of natural volcanic forcing in replicating multidecadal variations of the large-scale land precipitation.

Finally, it is speculated that shortcomings in the simulated global monsoon trend could be explained in part by the unrealistic SST variability in a model. A recent study by Zhou et al. (2008) has shown that when forced by historical sea surface temperatures covering the 1950–2004 period, the ensemble simulation with the NCAR Community Atmosphere Model, version 2 (CAM2), successfully reproduced the weakening tendency of global land monsoon precipitation. This decreasing tendency was mainly caused by the warming trend over the central-eastern Pacific and the western tropical Indian Ocean. Their work suggests that the significant change of global land monsoon precipitation may be deducible from the atmosphere's response to the observed SST variations. An observed warming in the global ocean is expected to increase evaporation from the sea surface to the atmosphere, hence enhancing precipitation over the ocean. However, the multidecadal variation of ocean heat content seen in the observations is underpredicted by the models (e.g., Gregory et al. 2004). Accordingly, the unrealistic simulations of the oceanic monsoon trend may be ascribable, to some extent, to this underestimated ocean warming trend. Another conceivable reason could be found in a relationship between global precipitation and El Niño–Southern Oscillation (ENSO). During ENSO events, precipitation is decreased over the global land (Dai et al. 1997), but increased over the global ocean (Dai and Wigley 2000). This implies that the large ENSO events occurred in the recent decades may contribute both to decreasing tendency in land monsoon rainfall and increasing wetness in oceanic monsoon precipitation over the globe. Performance of the CMIP3 models seems to be improved in capturing the frequency of occurrence and spatial structure of ENSO events when compared with their antecedent version; nevertheless, they are still unable to realistically simulate many aspects of ENSO variability (AchutaRao and Sperber 2006; Joseph and Nigam 2006), and, thus, could have difficulty in reproducing the global ENSO–rainfall linkage. Of course, the uncertainty contained in precipitation parameterization schemes could also be a critical impediment. Further research is needed in this regard to understand the role of SST variability on the global monsoon precipitation trend in a model.

Acknowledgments. We thank the anonymous reviewers for valuable suggestions. We also acknowledge the modeling groups for making their simulations available for analysis, the Program for Climate Model Diagnosis and Intercomparison (PCMDI) for collecting and archiving the CMIP3 model output, and the WCRP's Working Group on Coupled Modelling (WGCM) for organizing the model data analysis activity. The WCRP CMIP3 multimodel dataset is supported by the Office of Science, U.S. Department of Energy. This study is supported by Ministry of Environment of Korea as "The Eco-technopia 21 project." Bin Wang acknowledges the support from Climate Dynamics program of NSF Award ATM06-47995.

REFERENCES

AchutaRao, K. M., and K. R. Sperber, 2006: ENSO simulation in coupled ocean-atmosphere models: Are the current models better? *Climate Dyn.,* **27,** 1–15.

Ammann, C. M., G. A. Meehl, W. M. Washington, and C. S. Zender, 2003: A monthly and latitudinally varying volcanic forcing dataset in simulations of 20th century climate. *Geophys. Res. Lett.,* **30,** 1657, doi:10.1029/2003GL016875.

Annamalai, H., K. Hamilton, and K. R. Sperber, 2007: The South Asian summer monsoon and its relationship with ENSO in the IPCC AR4 simulations. *J. Climate,* **20,** 1071–1092.

Beck, C., J. Grieser, and B. Rudolf, 2005: A new monthly precipitation climatology for the global land areas for the period 1951 to 2000. German Weather Service Climate Status Rep. 2004, 181–190.

Biasutti, M., and A. Giannini, 2006: Robust Sahel drying in response to late 20th century forcings. *Geophys. Res. Lett.,* **33,** L11706, doi:10.1029/2006GL026067.

——, D. S. Battisti, and E. S. Sarachik, 2003: The annual cycle over the tropical Atlantic, South America, and Africa. *J. Climate,* **16,** 2491–2508.

Boer, G. J., G. Flato, M. C. Reader, and D. Ramsden, 2000: A

transient climate change simulation with greenhouse gas and aerosol forcing: Experimental design and comparison with the instrumental record for the twentieth century. *Climate Dyn.,* **16,** 405–425.

Broccoli, A. J., K. W. Dixon, T. L. Delworth, T. R. Knutson, R. J. Stouffer, and F. Zeng, 2003: Twentieth-century temperature and precipitation trends in ensemble climate simulations including natural and anthropogenic forcing. *J. Geophys. Res.,* **108,** 4798, doi:10.1029/2003JD003812.

Chang, C.-P., Z. Wang, J. McBride, and C.-H. Liu, 2005: Annual cycle of Southeast Asia–Maritime Continent rainfall and the asymmetric monsoon transition. *J. Climate,* **18,** 287–301.

Chase, T. N., J. A. Knaff, R. A. Pielke Sr., and E. Kalnay, 2003: Changes in global monsoon circulations since 1950. *Nat. Hazards,* **29,** 229–254.

Chen, M., P. Xie, J. E. Janowiak, and P. A. Arkin, 2002: Global land precipitation: A 50-yr monthly analysis based on gauge observations. *J. Hydrometeor.,* **3,** 249–266.

Covey, C., K. M. AchutaRao, U. Cubasch, P. Jones, S. J. Lambert, M. E. Mann, T. J. Phillips, and K. E. Taylor, 2003: An overview of results from the Coupled Model Intercomparison Project. *Global Planet. Change,* **37,** 103–133.

Dai, A., 2006: Precipitation characteristics in eighteen coupled climate models. *J. Climate,* **19,** 4605–4630.

——, and T. M. L. Wigley, 2000: Global patterns of ENSO-induced precipitation. *Geophys. Res. Lett.,* **27,** 1283–1286.

——, I. Y. Fung, and A. D. DelGenio, 1997: Surface observed global land precipitation variations during 1900–88. *J. Climate,* **10,** 2943–2962.

Douglas, M. W., R. A. Maddox, K. Howard, and S. Reyes, 1993: The Mexican monsoon. *J. Climate,* **6,** 1665–1677.

Gillett, N. P., A. J. Weaver, F. W. Zwiers, and M. F. Wehner, 2004: Detection of volcanic influence on global precipitation. *Geophys. Res. Lett.,* **31,** L12217, doi:10.1029/2004GL020044.

Gong, D.-Y., and C.-H. Ho, 2002: Shift in the summer rainfall over the Yangtze River valley in the late 1970s. *Geophys. Res. Lett.,* **29,** 1436, doi:10.1029/2001GL014523.

Gregory, J. M., H. T. Banks, P. A. Stott, J. A. Lowe, and M. D. Palmer, 2004: Simulated and observed decadal variability in ocean heat content. *Geophys. Res. Lett.,* **31,** L15312, doi:10.1029/2004GL020258.

Hansen, J. E., and M. Sato, 2001: Trends of measured climate forcing agents. *Proc. Natl. Acad. Sci. USA,* **98,** 14 778–14 783, doi:10.1073/pnas.261553698.

Hegerl, G. C., and Coauthors, 2007: Understanding and attributing climate change. *Climate Change 2007: The Physical Science Basis,* S. Solomon et al., Eds., Cambridge University Press, 663–745.

Hoerling, M., J. Hurrell, J. Eischeid, and A. Phillips, 2006: Detection and attribution of twentieth-century northern and southern African rainfall change. *J. Climate,* **15,** 3989–4008.

Huffman, G. J., and Coauthors, 1997: The Global Precipitation Climatology Project (GPCP) combined precipitation dataset. *Bull. Amer. Meteor. Soc.,* **78,** 5–20.

Joseph, R., and S. Nigam, 2006: ENSO evolution and teleconnections in IPCC's twentieth-century climate simulations: Realistic representation? *J. Climate,* **19,** 4360–4377.

Kalnay, E., and Coauthors, 1996: The NCEP/NCAR 40-Year Reanalysis Project. *Bull. Amer. Meteor. Soc.,* **77,** 437–471.

Kendall, M. G., 1955: *Rank Correlation Methods*. 2nd ed. Oxford University Press, 196 pp.

Kripalani, R. H., and A. Kulkarni, 2001: Monsoon rainfall variations and teleconnections over South and East Asia. *Int. J. Climatol.,* **21,** 603–616.

——, R. H., S. Inamdar, and N. A. Sontakke, 1996: Rainfall variability over Bangladesh and Nepal: Comparison and connections with features over India. *Int. J. Climatol.,* **16,** 689–703.

Lambert, F. H., P. A. Stott, M. R. Allen, and M. A. Palmer, 2004: Detection and attribution of changes in 20th century land precipitation. *Geophys. Res. Lett.,* **31,** L10203, doi:10.1029/2004GL019545.

——, N. P. Gillett, D. A. Stone, and C. Huntingford, 2005: Attribution studies of observed land precipitation changes with nine coupled models. *Geophys. Res. Lett.,* **32,** L18704, doi:10.1029/2005GL023654.

Lau, K.-M., and H. Weng, 2002: Recurrent teleconnection patterns linking summertime precipitation variability over East Asia and North America. *J. Meteor. Soc. Japan,* **80,** 1309–1324.

——, S. S. P. Shen, K.-M. Kim, and H. Wang, 2006: A multimodel study of the twentieth-century simulations of Sahel drought from the 1970s to 1990s. *J. Geophys. Res.,* **111,** D07111, doi:10.1029/2005JD006281.

Le Barbé, L., T. Lebel, and D. Tapsoba, 2002: Rainfall variability in West Africa during the years 1950–90. *J. Climate,* **15,** 187–202.

Legates, D. R., and C. J. Willmott, 1990: Mean seasonal and spatial variability in gauge-corrected, global precipitation. *Int. J. Climatol.,* **10,** 111–127.

Mechoso, C. R., and Coauthors, 1995: The seasonal cycle over the tropical Pacific in coupled ocean–atmosphere general circulation models. *Mon. Wea. Rev.,* **123,** 2825–2838.

Meehl, G. A., 1997: The South Asian monsoon and the tropospheric biennial oscillation. *J. Climate,* **10,** 1921–1943.

——, and J. M. Arblaster, 2002: The tropospheric biennial oscillation and Asian–Australian monsoon rainfall. *J. Climate,* **15,** 722–744.

——, C. Covey, B. McAvaney, M. Latif, and R. J. Stouffer, 2005: Overview of the Coupled Model Intercomparison Project. *Bull. Amer. Meteor. Soc.,* **86,** 89–93.

——, J. M. Arblaster, D. M. Lawrence, A. Seth, E. K. Schneider, B. P. Kirtman, and D. Min, 2006: Monsoon regimes in the CCSM3. *J. Climate,* **19,** 2482–2495.

Mitchell, T. D., and P. D. Jones, 2005: An improved method of constructing a database of monthly climate observations and associated high-resolution grid. *Int. J. Climatol.,* **25,** 693–712.

Murakami, T., B. Wang, and S. W. Lyons, 1992: Contrasts between summer monsoons over the Bay of Bengal and the eastern North Pacific. *J. Meteor. Soc. Japan,* **70,** 191–210.

Nicholson, S. E., 1993: An overview of African rainfall fluctuations of the last decades. *J. Climate,* **6,** 1463–1466.

Phillips, T. J., and P. J. Gleckler, 2006: Evaluation of continental precipitation in 20th century climate simulations: The utility of multimodel statistics. *Water Resour. Res.,* **42,** W03202, doi:10.1029/2005WR004313.

Ramachandran, S., V. Ramaswamy, G. L. Stenchikov, and A. Robock, 2000: Radiative impacts of the Mt. Pinatubo volcanic eruption: Lower stratospheric response. *J. Geophys. Res.,* **105,** 409–424.

Ramage, C. S., 1971: *Monsoon Meteorology.* Academic Press, 296 pp.

Rodwell, M. J., and B. J. Hoskins, 2001: Subtropical anticyclones and summer monsoons. *J. Climate,* **14,** 3192–3211.

Santer, B. D., and Coauthors, 2005: Amplification of surface temperature trends and variability in the tropical atmosphere. *Science,* **309,** 1551–1556.

——, and Coauthors, 2006: Forced and unforced ocean temperature changes in Atlantic and Pacific tropical cyclogenesis regions. *Proc. Natl. Acad. Sci. USA,* **103,** 13 905–13 910, doi:10.1073/pnas.0602861103.

Sato, M., J. E. Hansen, M. P. McCormick, and J. B. Pollack, 1993: Stratospheric aerosol optical depth, 1850–1990. *J. Geophys. Res.,* **98,** 22 987–22 994.

Wang, B., 1994: Climatic regimes of tropical convection and rainfall. *J. Climate,* **7,** 1109–1118.

——, and LinHo, 2002: Rainy season of the Asian–Pacific summer monsoon. *J. Climate,* **15,** 386–398.

——, and Q. Ding, 2006: Changes in global monsoon precipitation over the past 56 years. *Geophys. Res. Lett.,* **33,** L06711, doi:10.1029/2005GL025347.

——, and ——, 2008: Global monsoon: Dominant mode of annual variation in the tropics. *Dyn. Atmos. Oceans,* **44,** 165–183.

——, R. Wu, and K.-M. Lau, 2001: Interannual variability of Asian summer monsoon: Contrast between the Indian and western North Pacific–East Asian monsoons. *J. Climate,* **14,** 4073–4090.

Waple, A. M., and Coauthors, 2002: Climate assessment for 2001. *Bull. Amer. Meteor. Soc.,* **83,** S1–S62.

Xie, S.-P., H. Xu, N. H. Saji, Y. Wang, and W. T. Liu, 2006: Role of narrow mountains in large-scale organization of Asian monsoon convection. *J. Climate,* **19,** 3420–3429.

Yu, R., B. Wang, and T. Zhou, 2004: Tropospheric cooling and summer monsoon weakening trend over East Asia. *Geophys. Res. Lett.,* **31,** L22212, doi:10.1029/2004GL021270.

Zhang, P., S. Yang, and V. E. Kousky, 2005: South Asian high and Asian-Pacific-American climate teleconnection. *Adv. Atmos. Sci.,* **22,** 915–923.

Zhou, N. F., Y. Q. Yu, and Y. F. Qian, 2006: Simulations of the 100 hPa South Asian high and precipitation over East Asia with IPCC coupled GCMs. *Adv. Atmos. Sci,* **23,** 375–390.

Zhou, T. J., R. Yu, H. Li, and B. Wang, 2008: Ocean forcing to changes in global monsoon precipitation over the recent half century. *J. Climate,* **21,** 3833–3852.